Thermochromic VO2 for energy-efficient smart windows

Cui, Yuanyuan; Ke, Yujie; Liu, Chang; Chen, Zheng; Wang, Ning; Zhang, Liangmiao; Zhou, Yang; Wang, Shancheng; Gao, Yanfeng; Long, Yi

2018

Cui, Y., Ke, Y., Liu, C., Chen, Z., Wang, N., Zhang, L., . . . Long, Y. (2018). Thermochromic VO2 for energy-efficient smart windows. Joule, 2(9), 1707-1746. doi:10.1016/j.joule.2018.06.018

https://hdl.handle.net/10356/137055

https://doi.org/10.1016/j.joule.2018.06.018

Thermochromic VO_2 for Energy-Efficient Smart Windows

Yuanyuan Cui,[1,5] Yujie Ke,[2,5] Chang Liu,[2] Zhang Chen,[1] Ning Wang,[2,3]
Liangmiao Zhang,[1] Yang Zhou,[2] Shancheng Wang,[2] Yanfeng Gao,[1,*] Yi Long [2,4,*]

[1] *School of Materials Science and Engineering, Shanghai University, Shanghai 200444, China*

[2] *School of Materials Science and Engineering, Nanyang Technological University, 50 Nanyang Avenue, 639798, Singapore*

[3] *Shenzhen Institutes of Advanced Technology, Chinese Academy of Sciences, Shenzhen, 518055, China*

[4] *Singapore-HUJ Alliance for Research and Enterprise (SHARE), Nanomaterials for Energy and Energy-Water Nexus (NEW), Campus for Research Excellence and Technological Enterprise (CREATE), 138602, Singapore*

[5] *These authors contributed equally to this work*

** Correspondence: yfgao@shu.edu.cn (Yanfeng Gao), LongYi@ntu.edu.sg (Yi Long)*

Abstract

Rapid development of the thermochromic glazing technique promises next-generation architectural windows with energy-saving characteristics by intelligently regulating indoor solar irradiation *via* modulating their optical properties in response to the surrounding temperature. Vanadium dioxide (VO_2) is a promising material for energy-saving smart windows due to its reversible metal-to-insulator transition near room temperature, accompanying with large changes in its optical properties. This review provides a comprehensive overview of the application of VO_2 to smart windows with particular emphasis on recent progress from the electronic-, atomic-, nano- and micron- perspectives. The effects of intrinsic atomic defects, elemental doping, and lattice strain on VO_2 nanocrystals are examined. Nano- and microscale morphology engineering approaches are summarized aiming to enhance the thermochromic performance and impart practical multi-functionalities. Finally, the challenges and future directions of VO_2-based smart windows are elaborated to bridge the gap between the lab research and large scale practical applications.

Key words: Smart windows; Vanadium dioxide; Thermochromics; Insulator-to-metal transition; Optical modulation; Solar energy; Energy conservation.

Abbreviations and acronyms

ARC	Antireflection coating
at.%	Atomic percentage
ATO	Sb-doped SnO_2
AZO	Al-doped ZnO
CLETS	Co-based ligand exchange thermochromic system
CTAB	Cetyltrimethyl ammonium bromide
CTAV	Cetyltrimethylammonium vanadate
CVD	Chemical vapor deposition
DFT	Density functional theory
DOS	Density of states
EMT	Effective medium theory
FDTD	Finite difference time domain
FOS	Fluorooctyl triethoxysilane
FTO	F-doped SnO_2
HCL	Hydrochloric acid
HCP	Hexagonal-close-packed
HPC	Hydroxypropyl cellulose
IL-Ni-Cl	Ionic liquid-nickel-chlorine
IR	Infrared
LCA	Life cycle assessment
LCST	Lower critical solution temperature
LSPR	Localized surface plasmon resonance
M/R	Monoclinic/rutile
MCC	Monolayer colloidal crystal
MIT	Metal-to-insulator transition
N_2H_4	Hydrazine
NIR	Near-infrared
NLETS	Nickel-based ligand exchange thermochromic system
NP	Nanoparticle
PBG	Photonic band gap

PDMS	Polydimethylsiloxane
PE	Plasma etching
PEG	Polyethylene glycol
PET	Polyethylene terephthalate
PNIPAm	Poly-N-isopropylacrylmide
PS	Polystyrene
PU	Polyurethane
PVP	Polyvinylpyrrolidone
RhB	Rhodamine B
RI	Refractive index
SDS	Sodium dodecyl sulfate
SPR	Surface plasmon resonance
TEOS	Tetraethyl orthosilicate
T_{lum}	Average visible transmittance
VCl_2	Vanadyl dichloride
ΔT_{sol}	Solar energy modulation
τ_c	Phase transition temperature
ε_T	Thermal emissivity

1. Introduction

1.1 VO_2 and its metal-to-insulator phase transition

In recent years, both monoclinic (M) and rutile (R) phase vanadium dioxide (VO_2) have aroused great attention as a promising candidate for smart windows owing to the reversible metal-to-insulator transition (MIT) at a critical temperature of 68 °C (341 K).[1,2] This thermally induced phase transition is reversible, accompanied by a dramatic change in the optical properties in the near-infrared region from a low-temperature transparent state to a more blocking state at high temperatures, which imbues the VO_2-based window with the ability to regulate solar heat flux by responding to temperature automatically. Comparing with other thermochromic materials, VO_2 possess a relatively "silent" way with a negligible optical property change in visible spectrum range.[3] In fact, VO_2(M/R) is also a widely studied material in physical chemistry and condensed-matter physics because of its specific phase-transition features.[4-6]

The low-temperature insulating phase has a monoclinic structure (M, space group $P2_1/c$, a_M = 5.75 Å, b_M = 4.52 Å, c_M = 5.38 Å, β = 122.6°).[7,8] When the temperature is above 68 °C, this low-temperature insulating phase transforms to the high-temperature metallic phase, which displays a tetragonal structure (R, space group $P4_2/nm$, $a_R = b_R$ = 4.55 Å, c_R = 2.86 Å)[9] (Figure 1b). In VO_2(R), the vanadium atoms occupy the lattice point of the body-centered cubic structure and are located at the centers of the tilted VO_6 octahedra.[10] Four of the six oxygen atoms in the VO_6 octahedra are located closer to the vanadium atom, and the V-O bond distances are 1.92 and 1.93 Å, respectively. Chains of edge-sharing VO_6 octahedra have a corner-sharing arrangement with other VO_6 octahedra and are arranged linearly along the crystallographic *c*-axis, with a V-V distance of ~2.85 Å.[11] During the phase transition from VO_2(R) to VO_2(M), the vanadium atoms move along the V-V direction, resulting in the pairing and tilting of VO_6 octahedra in this direction.[12] Two distinct sets of long and short V-V distances (3.12 Å and 2.65 Å) exist as a result of the new positions of vanadium atoms in VO_2(M). The number of atoms in one VO_2(M) unit cell is 12, which is doubled as compared with the 6 atoms in one VO_2(R) unit cell.

To fully describe the phase-transition process of VO_2(M/R), a molecular picture based on relatively simple crystal-field theory is typically considered, as first proposed by Goodenough in 1971.[13] In brief and as shown in Figure 1a, in the VO_2(R), a wide π bond and a narrow π^* anti-bond are formed between the V^{4+} and O^{2-} orbitals,

and a $d_{//}$ nonbond is formed between adjacent V^{4+} orbitals along the crystallographic *c*-axis. Although the energy band of VO_2(R) is approximately 2.5 eV, the unfilled π^* and $d_{//}$ bands partially overlap, and the Fermi level falls at the point where the π^* and $d_{//}$ bands overlap, giving it metallic characteristics. When the temperature decreases, the tilting of the VO_6 octahedra enhances the π overlap between the V^{4+} and O^{2-} orbitals, thereby elevating the anti-bonding π^* level, whereas the $d_{//}$ bonds interact strongly in V-V pairs and then split into $d_{//}$ bonding and anti-bonding components. A band gap of ~0.7 eV is formed between the π^* and $d_{//}$ bands, leading to the formation of an insulating phase. Although this model exhibits several discrepancies from the experimental data, it can nevertheless qualitatively explain the nature of the phase transition in VO_2.

A fierce debate over the driving force of the VO_2 phase transition has persisted for several decades, with respect to whether the electron-electron correlation is strong enough to localize the electrons by forming a Mott-Hubbard insulator (Mott model) or whether structural distortions alone can induce the insulating phase (Peierls model).[14-18] Wentzcovitch *et al*. revealed a distorted monoclinic ground state to be in good agreement with the experimental findings and a nearly open gap with respect to charge excitations; thus, they believed that VO_2 may be more band-like than correlated.[18] This result was supported by Cavalleri *et al*., who employed ultrafast spectroscopy to construct a time-domain hierarchy between the structural and electronic effects, and found that the initiation of the metallic phase formation was prompted by hole photo-doping into the valence band of the insulator phase; therefore, the phase transition could be retarded with respect to hole injection and exhibits a bottleneck time scale.[19-21] Baum *et al*. used four-dimensional (4D) ultrafast electron microscopy to study the phase transition of VO_2 initiated by near-infrared excitation.[22] Their results suggest that the transition from the insulating phase to the metallic phase initially involves the expansion of the primary V-V bond with local displacements (on femtosecond and picosecond timescales), followed by long-range shear rearrangements (on a nanoseconds timescale and at the speed of sound), revealing a structural pathway and non-concerted transformation mechanism.

However, a number of phenomena, such as anomalously low conductivity and other unusual properties of the metallic phase, have suggested that the MIT phase transition involves strong electron-electron correlations (Mott model).[23] The fact that an intermediate monoclinic phase is insulating despite the presence of undimerized

V-V chains; and the dependence on excitation power observed experimentally indicates the sensitivity to the density of the excited carriers. The alternative Mott picture ascribes the presence of a band gap in VO_2(M) to strong electron-electron correlations, and the results of several experiments have indicated that if the thermally, optically or gate-voltage-induced excitation of carriers reaches a threshold, the metallic phase could develop even without a phase transformation.[11]

Yuan *et al.* recently reported measurements and calculations of the VO_2 phase transition and suggested that it might be both electronically and structurally driven,[24] in accordance with the stepwise non-concerted mechanism of photo-excitation-induced phase transition in VO_2 (M/R) proposed by Baum *et al.*[22] In brief, at least three distinct time scales emerge in the phase transition. The first step is the rapid dilation of the V-V bond (~307 fs); this step is followed by a slower, transverse motion of the VO_6 octahedra that locally rearrange to adopt a more rutile-like geometry (~9.2 ps) and a subsequent and far slower motion (~100 ps) that is ascribed to shear movements propagating at the speed of sound. When the phase transition is approached after the three mentioned steps, a spontaneous Peierls distortion would start initially for the cation chains. Finally, the extent of the distortion increases before the Peierls distortion spreads to the orthogonal chains.

1.2 Optical performance

Among the issues concerning VO_2-based thermochromic windows, optical performance is the most important because it directly determines the energy-conservation efficiency of the windows. The optical performance of a VO_2-based thermochromic window can be mainly characterized in terms of its luminous transmittance (T_{lum}, 380-780 nm), solar energy modulation ability (defined as ΔT_{sol}, the difference in solar-energy transmittance T_{sol} before and after the phase transition, which is 240-2500 nm), These quantities are calculated as follows:

$$T_i = \int \phi_i(\lambda) T(\lambda) d\lambda \Big/ \int \phi_i(\lambda) d\lambda \quad (1)$$

$$\Delta T_{sol} = T_{sol}(T < T_c) - T_{sol}(T > T_c) \quad (2)$$

where $T(\lambda)$ represents the transmittance at wavelength λ, i denotes lum or sol, $\phi_{lum}(\lambda)$ is the standard luminous efficiency function for vision (380-780 nm), and $\phi_{sol}(\lambda)$ is the solar irradiance spectrum at air mass 1.5 (corresponding to the sun standing 37° above the horizon).[25] For simplicity, all T_{lum} values presented in this review represent the

average of the T_{lum} values at low and high temperatures.

Both high T_{lum} and ΔT_{sol} are important as the former can save lighting while the latter determines the energy-conservation efficiency of VO_2-based thermochromic windows. However they have a trade-off relationship, meaning that it is difficult to improve both to an acceptable value, therefore most studies of thermochromic devices have focused on such attempt. For a continuous VO_2 thin film, the T_{lum} and ΔT_{sol} are limited and are unsatisfactory for practical usage. Reported solutions have involved three different approaches: optimization of the optical thin films, design of the film microstructure and formation of nanocomposites.

Another important parameter to characterize the energy-conservation efficiency of VO_2-based smart windows is the thermal emissivity (ε_T), which is refferred as the ratio of energy radiated by the windows to energy radiated by a blackbody at a defined temperature.[26] In thermal equilibrium conditions, the absorptivity of a subjuect is equal to its emissivity. Therefore, a blackbody absorbs all electromagnetic radiation that falls on it and shows ε_T=1, whereas a perfect reflector reflects all electromagnetic radiation and presents ε_T=0. The value of ε_T lies between 0 and 1. Generraly, ε_T is calculated *via* weighting the film reflectance with the black body emission spectrum from 4.5 to 25 mm as follows:

$$\varepsilon_T = \sum_{4.5}^{2.5} G_T(\lambda) E(\lambda) \Delta\lambda \qquad (3)$$

where $G_T(\lambda)$ is the normalized relative spectral distribution of black body radiation at temperature T (T is chosen to be 20 °C according to CNS GB/T 1895.2-2002). $E(\lambda)$ refers to the emittance, *i.e.*, the fraction of the black-body radiation.

There are several recently published review papers. Gao *et al.* specifically discussed the VO_2 in thermochromic glass application *via* solution processes.[2] Li *et al.* concluded the hydrothermal method and the transformation of VO_2(M) from its polymorphs.[27] Wu and Xie *et al*. emphasized the engineering microstructures of VO_2 with control of its electrical properties.[28] Jiang and Yu *et al.* outlined the deposition methods and the progress in performance enhancement.[29] Wang *et al.* summarized the chemical vapor deposition (CVD) deposition of VO_2 in energy conservation and storage.[30] Granqvist's group focused on the state of the art for VO_2-based thin films and nanocomposites.[31] Few of them focus on the theoretical simulations and experimental works regarding the structure/property relationship from atomic, nano-,

micron- perspectives, which may provide a comprehensive and insightful guidance of VO_2-based smart windows.

In this review, the progress in VO_2-based smart windows is overviewed, from the band structure designing at the electronic and atomic scales to morphology engineering from nano to micro-scales (Figure 1). The second section discusses the effects of intrinsic atomic defects, elemental doping, and lattice strain on the electronic and atomic structures of VO_2. Subsequently nano and microscale engineering methods to enhance the performance of smart windows are discussed, including incorporating particles, tuning the porosity, designing nanocomposites, developing biomimetic patterns, creating grids, and applying multifunctional antireflection coatings,(Figure 1c). Lastly, challenges and future directions are shared. We hope that this work may inspire more innovative progress and accelerates the development of this technique from the lab to industry (Figure 1d-e).

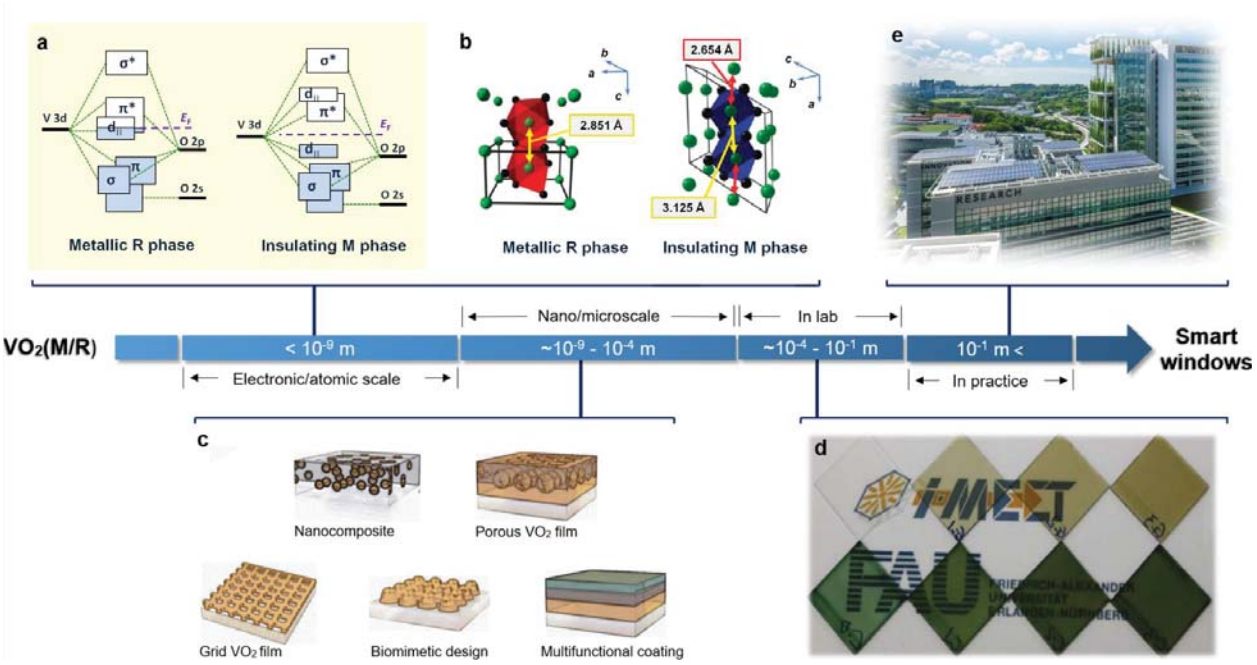

Figure 1. Overview of the development of VO_2 smart windows from the electronic/atomic scale to the nano/microscale, then to in-lab tests, and finally their practical application in architecture. (a) Band structures of the metallic R and insulating M phases of VO_2 depicted by molecular orbital diagrams. (b) Schematic of the atomic structures of the high-temperature metallic tetragonal phase R and the low-temperature insulating monoclinic phase M. The V-V distances in each crystal structure are highlighted. (c) Nano/microengineering toward performance enhancement. (d) Photographs of VO_2-based thermochromic samples in the lab. (e) Photographs of architectural windows in practice. Figures reproduced with permission from: **a-b**, ref.[11], American Chemical Society; **d**, ref.[32], Wiley.

2. Electronic and atomic structure of VO_2

In this section, the intrinsic point defects, dopant and strain influence on VO_2 will be overviewed with the special focus on reducing the phase transition temperature (τ_c) of VO_2 from electronic and atomic perspectives.

2.1 Intrinsic point defects

Intrinsic point defects, such as cation nonstoichiometry or oxygen vacancies, always exist in metallic oxides and are desirable or even crucial in some cases to impact certain properties.[33] Recently, the introduction of oxygen vacancies into VO_2 presents great potential in reducing its τ_c and even alters its optical and electrical properties.[13,34]

The underlying mechanism can be interpreted as follows: The reaction to form one oxygen vacancy can be expressed as $O_o^x \rightarrow V_o + 2e + 0.5O_2$,[35] where the two resulting electrons are trapped by V^{4+} sites and then lead to lower valence states of V. This further induces multiple donor levels below the π^* band, resulting in narrowed band gap for VO_2(M) (Figure 2a-c),[35,36] which is closely correlated with the τ_c and the optical properties of VO_2.

To probe the effect of oxygen vacancies in VO_2, Chen *et al.* conducted first-principles calculations on the VO_{2-x} crystalline models.[37,38] Their simulations revealed that the oxygen vacancies give rise to an enhanced concentration of electrons, and the calculated τ_c of $VO_{1.984}$ and $VO_{1.969}$ are reduced to 226 and 142 K, respectively (Figure 2d), which are much lower than that of pure VO_2 (340 K).[37,38] In addition, the calculated absorption coefficients ($a(\omega)$) of VO_2 and $VO_{1.984}$ (Figure 2e) showed that after the introduction of oxygen vacancies, a new peak appeared in the low-energy region at approximately 0.4 eV in VO_{2-x}(M), which could improve the sunlight utilization in the infrared region.[37] The calculated reflectivity spectra of $VO_{1.984}$ (Figure 2f) illustrates that the reflectivity ($R(\omega)$) of $VO_{1.984}$(M) and $VO_{1.984}$(R) are higher than those of pure VO_2, suggesting that the introduction of oxygen vacancies into VO_2 can improve the reflectivity in the infrared region.[38]

Experimentally, oxygen vacancies are frequently introduced by adjusting the oxygen flow ratio during the process of preparation. For instance, Zhang *et al*. fabricated a series of VO_2 nanobeams and found that oxygen vacancies can stabilize the VO_2(R) phase at 103 K, suppressing of the phase transition by 238 K (Figure 2g).[39] Zhang *et al*. also reported that the presence of oxygen vacancies induced by the

oxygen pressure decreases the τ_c.[40] Jiang plotted the transmittance spectrum (Figure 2h) and absorptivity spectrum (Figure 2i) of the VO_2 thin films at different oxygen flow ratios and found that the low-temperature VO_2(M) phase showed a gradual decrease in the near-infrared (NIR) transmittance but increased absorptivity with decreasing oxygen flow ratio.[41] Oxygen vacancies can also be introduced by loading an electric field on VO_2. For instance, Jeong *et al*. suppressed the phase transition below 5 K in VO_2 through the formation of electric field-induced oxygen vacancies.[42] Later, Chen *et al*. examined the formation, diffusion, and recovery of oxygen vacancies in an electrolyte-gated VO_2 crystal lattice by temperature-dependent *in situ* resistance measurements and first-principles calculations.[43] Their results showed that oxygen vacancies result in the deformation of crystal structures and induce polarization charges, therefore modulating the d-orbital occupancy in VO_2.[43]

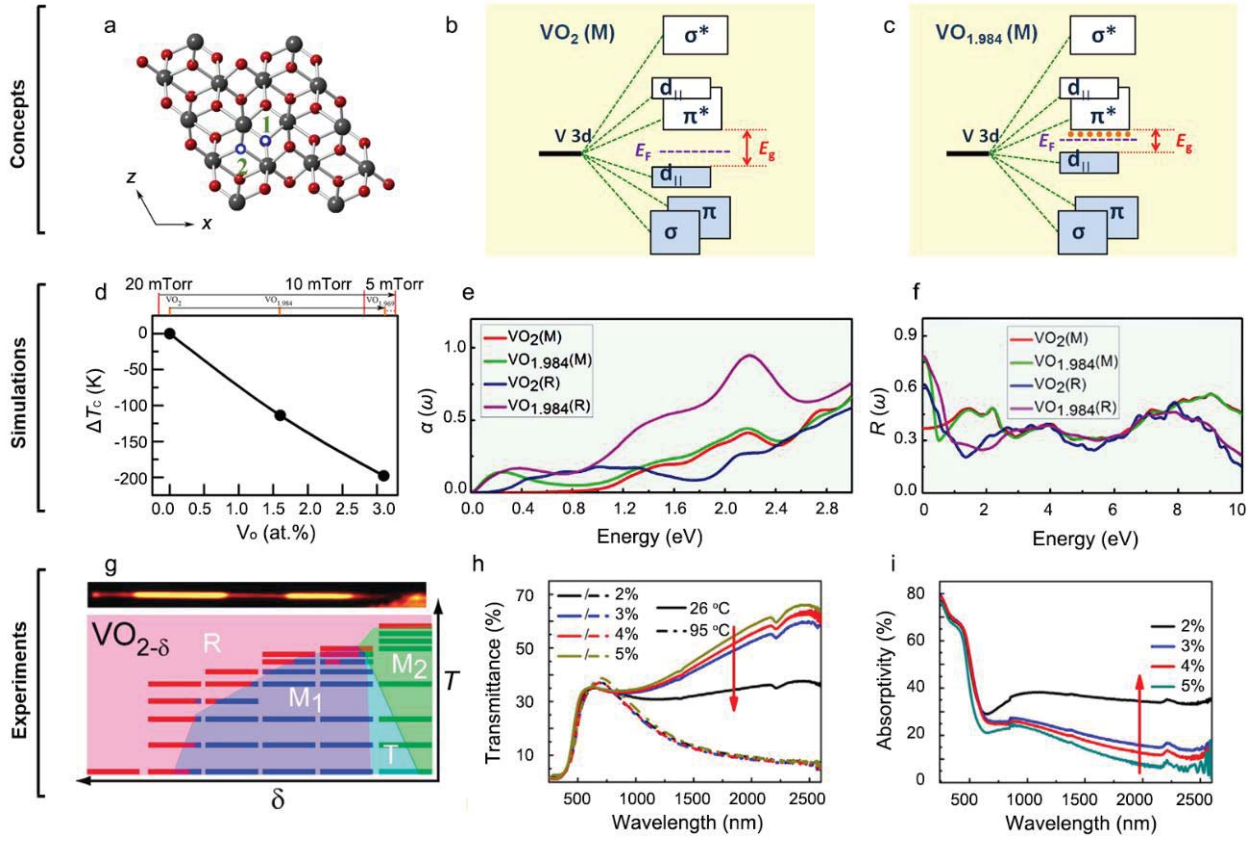

Figure 2. The effect of oxygen vacancies on the thermochromic performace of VO_2. (a) Side view of the VO_2(M) crystal structure with oxygen vacancies, the small red spheres represent oxygen atoms, and the large gray spheres represent vanadium atoms, O1 and O2 represent two types of oxygen vacancies in VO_2(M), and O1 site is energetically favorable over the O2 site. Outline of the band scheme of (b) VO_2(M) and (c) $VO_{1.984}$(M). (d) Reduction of the transition temperature with an increase in the oxygen vacancy concentration. (e) The absorption coefficients ($\alpha(\omega)$) of VO_2 and $VO_{1.984}$ given in 10^5 cm^{-1}. (f) The reflectivity ($R(\omega)$) spectra of VO_2 and $VO_{1.984}$. (g)

Structural phase diagram showing the impact of annealing on the transition temperature. (h) Transmittance and (i) absorptivity spectra of VO_2 films fabricated with different oxygen flow ratios. Figures reproduced with permission from: **a**, ref.[36], American Institute of Physics; **d-f**, ref.[38], Royal Society of Chemistry; **g**, ref.[39], American Chemical Society; **h-i**, ref.[41], Elsevier.

2.2 Elemental doping

Elemental doping is a process that intentionally introduces other element(s) into a pure material to modify its electrical or optical properties. For VO_2, elemental doping is one of the conventional strategies to tailor its τ_c and optical properties. Presently, more than 60 elements have been investigated as dopants for the VO_2 system either experimentally or theorectically.[44-95] The effects of some doping elements are summarized in Table 1.

The electronic phase transition in VO_2 is proposed to be accompanied by a (nearly) simultaneous structural phase transition between the VO_2(R) and VO_2(M) phase.[24,96] If the energy barrier across the phase transition could be lowered by doping, τ_c would decrease. Accordingly, the selection of the doping element is commonly based on two aspects: increasing the carrier concentration to accelerate the electronic phase transition, or introducing distortion into the atomic structure to assist the structural phase transition.

Firstly, the doping element should increase the carrier concentration of VO_2. When the doping element serves as the donor or acceptor in VO_2, it injects its electrons or holes into the electronic structure of VO_2, which increases the carrier concentration in the system. Because the electronic phase transition of VO_2 is a debatably typical Mott phase transition,[97] the increased carrier concentration lowers the energy barrier across the phase transition, thus decreasing the τ_c. There are two doping strategies to increase the carrier concentration. One is to insert smaller-sized doping atoms, such as H,[92] Li,[98] Na[98] and B[75] into the interstitial sites of VO_2 (Figure 3a). For instance, hydrogen is the lightest atom, which possesses one electron in its outermost orbital. When doped into VO_2, the H atoms are located at the interstitial sites and inject their electrons into the VO_2 system (Figure 3b).[57,77,92] Gao *et al.* presented that H efficiently reduces the τ_c by 38 K/at% H (Figure 3c).[92] The other strategy to increase the carrier concentration is to substitute the V sites with high-valance element (Figure 3d) such as W,[99,100] Nb[56,80] and Mo.[55,101] The doped W atoms have been shown to inject some of their electrons into the V 3d valence bands and reduce the τ_c by 20-26 K/at.%,[99] He *et al*. gained the results that the optical band gap can be narrowed from 0.65 to 0.54 eV by increasing the W-doping concentration (Figure 3e-f).[89]

Secondly, the doping element should introduce structural distortion into VO_2, especially along the V-V chains. VO_2(M) and VO_2(R) belong to the space groups

*P*21/*c* and *P*42/*mnm* respectively, and their apparent difference lies in the lengths of the V-V bonds, which are constant in VO_2(R) but alternatively varying in VO_2(M) (Figure 3g).[7,8] If a dopant causes the V-V distances in VO_2(R) to alternatively change (Figure 3h) thereby resembling that of VO_2(M), the dopant will lower the τ_c. For instance, Zhang *et al*. reported that Be-doped VO_2(R) displays structural distortion around the Be atom, where the V-V chains present dimerization similar to those in VO_2(M).[68] Through first principles calculations, they predicted that the reduction of τ_c in the Be-doped VO_2 is as large as 58 K/at.%.[68] In addition to the V-V distance, the lattice parameters can also be modified by dopants, which will influence the τ_c. Sun *et al*. proposed that if a dopant can introduce changes in the lattice parameters of VO_2(M) to resemble those of VO_2(R), the dopant will decrease the τ_c.[78] They conducted density functional theory (DFT) calculations and found that the τ_c decreases with the expansion of the lattice and decrease in the β-angle of VO_2(M) with transition metal doping (Figure 3i).[78]

Variation in the carrier concentration and structural distortion frequently occurs together, as the doping element either occupies the interstitial sites or substitutes the lattice site of V or O atoms, leading to variations in both the electronic and atomic structures of VO_2.

It was recently reported that elemental doping can also modify the emissivity, which is another important parameter to characterize the energy-conservation efficiency of VO_2.[102] For instance, Liu *et al*. synthesized pure VO_2 thin film on fused quartz substrate by using the sol-gel process, finding that the emissivity of VO_2 film (thickness of 900 nm) can be changed by 0.6 in the 7.5-14 μm region across the phase transition. They then prepared W-doped VO_2 films through the same process followed by the post-annealing.[102] Their results indicated that the emissivity of W-doped VO_2 thin films was decreased gradually with increasing doping amount of W, and the emissivity of VO_2 thin film (doping level of 4 at.% W) dropped to 0.4 when the temperature is high then 30 °C.[102]

Table 1 Elemental doping effects on the thermochromic performance of VO_2 thin films

Group	Dopant	Doping level	T_{lum} (%)	ΔT_{sol} (%)	$d\tau_c/dx$ (°C/at.%)	Ref.
IA	H	3%	\	\	−38	Simul.[92]
	Li	3%	\	\	−43	Simul.[98]
	Na	3%	\	\	−49	Simul.[98]
	K	3%	\	\	−94	Simul.[98]
IIA	Be	3%	\	\	−58	Simul.[68]
	Mg	5%	82.1	4.8	−3	Expt.[86]
	Ca	1.3%	\	7.6	\	Expt.[91]
	Sr	9.6%	54.3	5.0	\	Expt.[91]
	Sr	6.8%	50.3	6.5	\	Expt.[91]
	Ba	8.3%	\	7.5	\	Expt.[91]
IIIA	B	\	\	\	−83	Simul.[75]
VIIA	F	2.93%	48.7	10.7	−11.3	Expt.[71]
Transition Metal	W	2%	45.1	6.9	−20	Expt.[100]
	Mo	2%	\	\	−11	Expt.[55]
	Nb	2%-3%	\	\	−7.8	Expt.[56]
	Zr	9.8%	60.4	14.1	−0.4	Expt.[103]
	Ti	1.1%	53	17.2	0	Expt.[72]
Rare Earth	Eu	4%	54	6.7	−6.5	Expt.[83]
	Tb	4%	65.9	4.6	−1.5	Expt.[104]
	La	4%	50.1	10.3	−1.1	Expt.[105]
Co-Doping	Mg+W	4% Mg + 2% W	81.3	4.3	−5.5	Expt.[86]
	F+W	2.1% F + 1.8% W	\	\	−17.4	Expt.[53]
	Zr+W	8.5% Zr + 0.6% W	56.4	12.3	−1.3	Expt.[103]
	Mo+W	1.02% Mo + 0.36% W	\	\	−23	Expt.[61]

Note: "\" means data not available.

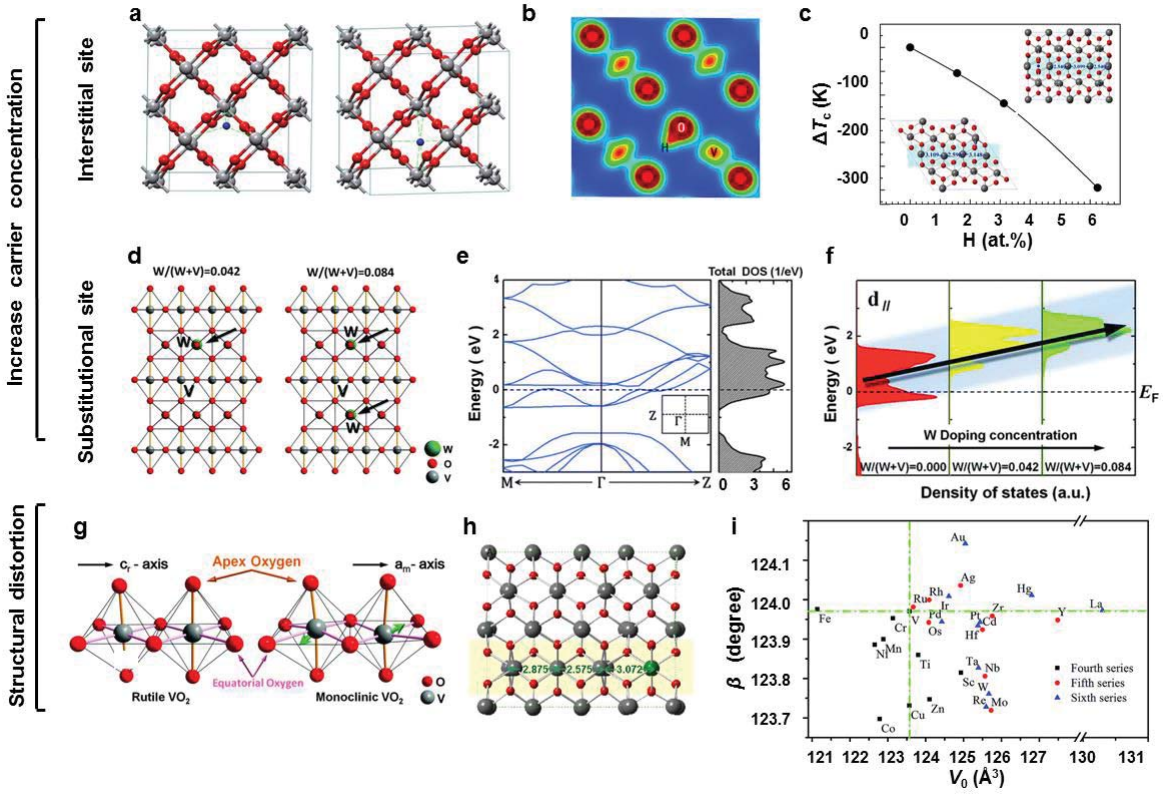

Figure 3. The effect of elemental doping on the thermochromic performace of VO_2. (a) The location of H atom at the tetrahedral (left) and octahedral (right) interstitial site in VO_2, where H, V and O atoms are indicated by blue, gray and red spheres, respectively. (b) The electron density of the (0 0 1) plane in H-doped VO_2(R). (c) The dependence of the transition temperature reduction on the H-doping concentration. (d) The location at which a W atom substitutes the V atom in VO_2, where the W, V and O atoms are indicated by green, gray and red spheres, respectively. (e) Band structure and total density of states (DOS) of pure VO_2(R). (f) Partial DOS of the $d_{//}$ orbital in VO_2 with different W concentrations. (g) Atomic structures for VO_2(R) and VO_2(M) during phase transition, the green arrows indicate the directions in which the V atoms. (h) Sb dopant causes the V-V distances to alternatively vary in VO_2(R). (i) Distribution of transition metal doped VO_2(M) with respect to the volume and β angle. Figures reproduced with permission from: **a-c**, ref.[92], Royal Society of Chemistry; **d-g**, ref.[89], Royal Society of Chemistry; **h**, ref.[106], Elsevier; **i**, ref.[78], Royal Society of Chemistry.

2.3 Impacts of strain on τ_c

In 1969, Ladd *et al*. first reported that the hydrostatic pressure only has a slight impact on the τ_c of VO_2, with a rate of $d\tau_c/dP$ = 0.6 K/GPa, whereas uniaxial stress along the *c*-axis displays a noticeable effect, with a rate of $d\tau_c/dP$ = −12 K/GPa.[107] Since then, there has been a great interest in scaling the τ_c of VO_2 by loading strain or pressure on it.[39,108-111]

The τ_c is known to be closely correlated with the length of the *c*-axis (adjacent V-V distance) of VO_2 (Figure 4a). Loading compressive strain along the *c*-axis leads to further overlap of the d orbitals and the increasing width of the d band, thus stabilizing the VO_2(R) phase and reducing the τ_c. Two strategies are commonly used to apply strain to VO_2: bending suspended VO_2 beams along the length direction (Figure 4b)[23,112] and depositing VO_2 thin films on certain substrates to introduce an interaction between the film and substrate (Figure 4c).[113-118]

Experimentally, Cao *et al*. fabricated single-crystalline VO_2 beams followed by three-point bending along the length direction of the beams.[112] They constructed a phase-strain diagram and found that the τ_c decreased upon loading compressive strain on the VO_2 beams and increased upon loading tensile strain (Figure 4d).[112] Wei *et al.* patterned a series of vanadium metal contacts onto a VO_2 nanobeam followed by removing the underlying SiO_2 to suspend the nanobeam sections between the contacts and subsequently cycled it between room temperature and 120 °C.[23] They also sketched a phase-pressure diagram of VO_2 (Figure 4e), illustrating reduced τ_c under compressive strain and enhanced τ_c under tensile strain.[23] Muraoka *et al*. prepared VO_2 thin films by pulsed laser deposition on TiO_2 (0 0 1) and (1 1 0) substrates and found that the τ_c decreased to 300 K for the VO_2 film grown on TiO_2 (0 0 1), because the *c*-axis was shortened due to the epitaxial stress, whereas the τ_c increased to 369 K for the VO_2 film grown on TiO_2 (1 1 0), because the *c*-axis was elongated, as illustrated in Figure 4f.[115,116]

Recent computational simulations confirmed the combined impacts of strain and doping (or O-vacancies).[37,68,92] Cui *et al*. conducted first-principles calculations and identified that a 2% compressive strain on H-doped VO_2 (with a doping level of 1 at.%) would decrease the τ_c by 51 K (Figure 4g).[92] Zhang *et al*. presented that the τ_c of Be-doped VO_2 could be further reduced by uniaxial strain, which is in close correlation with the dimerization of V-V chains in rutile VO_2 (Figure 4h).[68] Chen *et al*. found that a 2% compressive strain on pure VO_2 corresponds to a reduction in τ_c of

31.16 K, whereas the reduction increased to 56.74 K when the same compressive strain was loaded on the O-deficient VO_{2-x} (Figure 4i).[37]

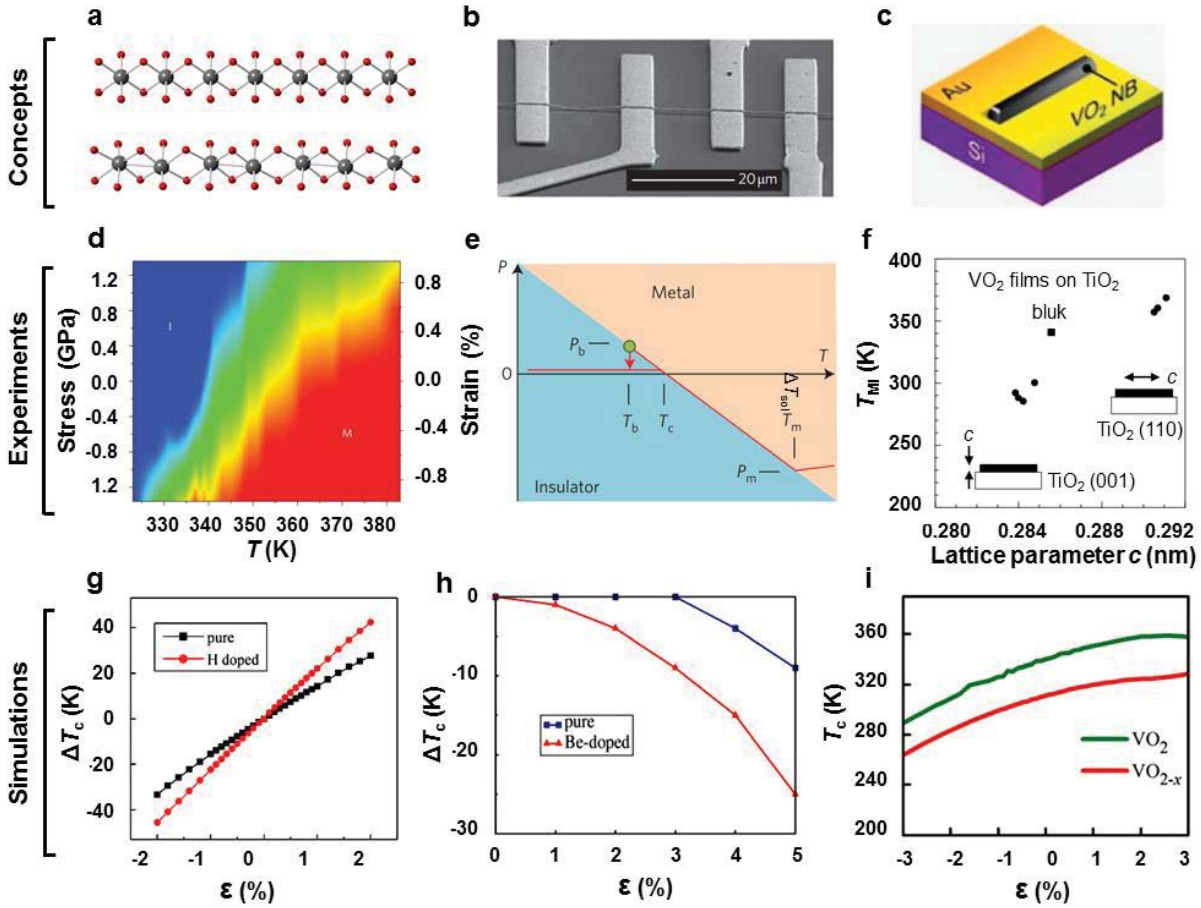

Figure 4. The effect of strain on the phase transition temperature of VO_2. (a) V-V chains for pure VO_2(R) (upper) and VO_2(M) (lower), the small red spheres for oxygen atoms and the large gray spheres for vanadium atoms. (b) Scanning electron microscopy (SEM) image of the suspended VO_2 nanobeam device. (c) Schematic illustration of individual VO_2 nanobeams on a Au-coated Si substrate. (d) Phase diagram of VO_2(M) fraction with respect to temperature, uniaxial stress and strain. (e) Phase diagram of metallic and insulating VO_2 phases with respect to temperature and strain. (f) τ_c *vs* the lattice parameter *c* for VO_2 films deposited on TiO_2(110) and TiO_2(001) substrates. (g) Relationship between the strain and the reduction of τ_c in pure and H-doped VO_2. (h) Relationship between the strain and the reduction of τ_c in pure and the Be-doped VO_2. (i) Dependence of τ_c on the strain loaded on VO_{2-x}. Figures reproduced with permission from: **b**, ref.[23], Nature Publishing Group; **c**, ref.[118], Royal Society of Chemistry; **d**, ref.[112], Nature Publishing Group; **e**, ref.[23], Royal Society of Chemistry; **f**, ref.[116], Elsevier; **g**, ref.[92], Royal Society of Chemistry; **h**, ref.[68], Royal Society of Chemistry; **i**, ref.[37], Royal Society of Chemistry.

3. Nano- and micro-structure of VO_2

Nano- and microscale morphology engineering approaches on VO_2 will be elaborated aiming to enhance its thermochromic properties, namely achieving large T_{lum} and ΔT_{sol} simultaneously.

3.1 VO_2 crystals

Monodisperse, nano-size, high crystallinity VO_2(M/R) particles are more favorable because these particles can be dispersed in the aqueous solvent and be cast into films with good visible transmittance and regulation ability of infrared light. A number of methods, summarized in Table 2, have been developed to obtain VO_2(M/R) particles. Gas phase reactions, such as chemical vapor deposition (CVD),[119] pulsed laser deposition (PLD),[120,121] and solid phase reaction, such as thermolysis,[122,123] and thermal reduction,[124] have long been regarded as the exclusive strategy to obtain VO_2 particles. For the gas or solid phase preparation methods of VO_2 particles, the readers can be referred to the well-written review paper.[121] The experimental conditions of gas or solid phase reactions frequently require precisely scaled inert gas atmospheres, rigidly controlled temperatures, post treatment, and long synthesis time. Over the past decade, a number of liquid phase reaction approaches have been reported, such as the hydrothermal method,[125-127] seeded growth method,[128] precursors transformation method,[129,130] and direct combustion method.[131] According to the transformation path, the methods to obtain VO_2(M/R) particles are divided into intermediate phase transformations, redox reactions, and one-step reactions.

Intermediate phase transformation is the main strategy to obtain VO_2(M/R) particles before the discovery of one-step reaction. Most studies on intermediate phase transformation focus on the fabrication of VO_2(B) nanoparticles followed by thermal treatment to transform VO_2(B) to VO_2(R) at elevated temperature.[132-138] For instance, Kam *et al*. first synthesized VO_2(B) nanorods through the hydrothermal method and then obtained VO_2(M) nanorods by thermal treatment of the metastable VO_2(B) at 700 °C in N_2 atmosphere.[133] In addition to the transformation from VO_2(B), Zhang *et al*. reported the synthesis of belt-like VO_2(M) particles through the transformation of VO_2(A) to VO_2(M).[137] Liu *et al*. discovered a new metastable phase, VO_2(D), which could guide the formation of VO_2(R/M) through a structural transition from VO_2(D) to VO_2(R).[138] Wu *et al*. reported a novel transformation pathway from the goethite VOOH to VO_2(P) to VO_2(R), with each step taking less than one minute, realizing an alternative ultrafast transformation to VO_2(M) (Figure 5a-c).[130] The intermediate

phase transformation method has two weaknesses. One is that the VO_2(M/R) particles obtained from intermediate phase transformation usually present the belt-like or rod-like morphologies, which are unfavorable for dispersion in the aqueous solvent. The other weakness is that the transformation typically requires a high temperature (>400 °C) and a long transformation time to obtain the fully transformed VO_2(M/R) phase.

Redox reaction is another strategy to prepare VO_2(M/R) particles, and V_2O_5 is usually the raw materials. V_2O_5 can be reduced to VO_2 by supplementary reducing agents (*e.g.*, $H_2C_2CO_4$, amine, alcohols, and N_2H_4) in hydrothermal/solvothermal reactions[139-142] or in a reductive atmosphere during high-temperature annealing.[124] For instance, Liu *et al*. reported that the VO_2(M) nanosheets (Figure 5d) were obtained by the solvothermal reaction and subsequent heat treatment of a the mixture of commercial V_2O_5 powder and absolute EtOH in a high-purity N_2 atmosphere.[140] Qi *et al*. employed the thermal reduction of V_2O_5 in ammonia gas to synthesize high-purity VO_2(M) particles (Figure 5e).[124] Chen *et al*. demonstrated a method to fabricate VO_2(R) particles through an electrochemical process using V_2O_5 as the cathode; after precisely controlling the electrical discharging currents, V^{5+} is reduced to V^{4+}, and VO_2(R) particles are obtained.[131,143] Wu *et al*. obtained VO_2(M) particles by directly combusting an ethanol solution containing $VO(acac)_2$ (ac = acetylacetonate) in a confined space,[131] which provided not only sufficient energy but also necessary reductive atmosphere to maintain the +4 valence state of vanadium, contributing to the formation of thermodynamically stable VO_2(R) (Figure 5f). The redox reaction method has two weaknesses: the impurity of the product and the toxicity of V_2O_5.

One-step reaction is regarded as an effective strategy to fabricate VO_2(M/R) particles with high crystallinity and at low cost. In 2008, Gao's group reported for the first time the synthesis of snowflake-shaped single-crystal W-doped VO_2 nanoparticles through a one-step hydrothermal reaction (Figure 5g-h).[125] Later, Ji *et al*. found that H_2SO_4 could serve as a morphology control agent in the same reaction system, so that VO_2 nanorods could be obtained directly from the one-step hydrothermal reaction (Figure 5i), and these nanorods presented excellent thermochromic properties with decreased τ_c and narrowed hysteresis.[126] In 2011, Gao *et al*. extended the above research and found that the τ_c was closely correlated with the sizes of VO_2(M) nanobumps with a critical size of 13.0 nm (Figure 5j).[127] Gao *et al*.[127] developed a new approach to modulate the τ_c in VO_2 systems *via* controlling the

nanoparticle size. Although the one-step hydrothermal method proposed by Gao *et al*. was powerful and could be employed to prepare pure and thermodynamically stable VO_2(M) nanoparticles in large quantities, the prepared VO_2(M) particles displayed snowflake-like aggregation with oriented growth, hindering their dispersion in matrix materials. In 2012, Gao *et al*.[144] proposed a doping strategy to simultaneously control the morphologies and sizes of VO_2 nanoparticles. Using a one-step hydrothermal method, Sb-doped VO_2(M) nanoparticles with controllable sizes were prepared (Figure 5k-m). These nanoparticles exhibited obvious phase-transition characteristics when dispersed in aqueous solvent, and the foils fabricated by casting the VO_2(M) nanoparticles illustrated outstanding optical properties.[144] Very recently, Ji *et al*. prepared uniform VO_2 nanoparticles by the one-step hydrothermal method, finding the tunability of emissivity of VO_2 nanoparticles in both mid- and far-IR thermal atmospheric windows for the first time.[145]

Table 2 Summary of the preparation methods of VO_2 particles

Category	Preparation method	Advantage	Disadvantage	Particle size	Particle shape	Ref.
Solid phase reaction	thermal reduction	massive production and low cost	impurity of the product, rigid experimental conditions, and toxicity of V_2O_5	micro	rhombohedral	[124]
	thermolysis	massive production and low cost	poor stability of the product, aggregation of particle	micro	irregular	[122]
Gas phase reaction	pulsed laser deposition	precise control of size and shape	rigid experimental conditions	micro/nano	rod	[120]
	chemical vapor deposition	high crystallinity	low yield, dependence on the substrates	nano	wire	[119]
Liquid phase reaction	hydrothermal method	high crystallinity and low cost	difficulty in dispersing particles in matrix materials	nano	snowflake	[125]
	seeded growth strategy	controllability of crystal growth	\	nano	star	[128]
	precursor transformation	time-saving	low yield	\	\	[130]
	direct combustion	time-saving	low yield	micron/nano	irregular	[131]

Note: "\" means data not available.

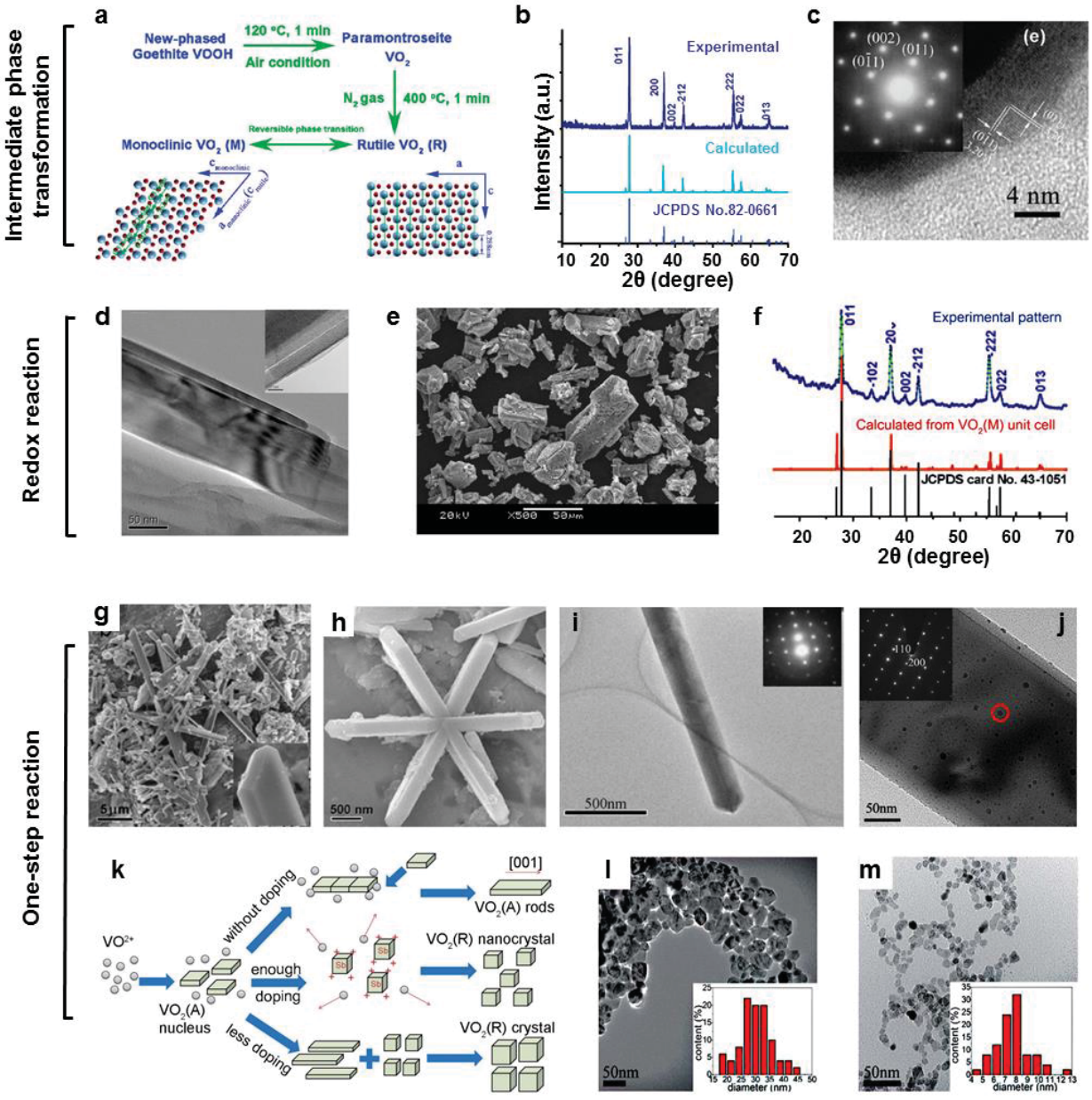

Figure 5. Different transformation paths to obtain VO_2(M/R) particles. (a) Illustration of the crystallographic transformation from the goethite VOOH to paramontroseite VO_2 to VO_2(M/R). (b) Experimental, calculated, and standard (JCPDS card No. 82-0661) XRD patterns of VO_2(M) crystals. (c) High-resolution transmission electron microscopy (HRTEM) image captured on the edge of a VO_2(M) nanoparticle and the corresponding and selected area electron diffraction (SAED) pattern (inset). (d) HRTEM image of VO_2(M) nanosheets fabricated from V_2O_5 powder and absolute EtOH in a high-purity N_2 atmosphere. (e) SEM image of the VO_2(M) particles obtained by thermal reduction of V_2O_5 in ammonia gas. (f) XRD pattern of the VO_2 particles obtained by direct confined-space combustion. (g) Field-emission SEM images of the VO_2 powders. (h) Snowflake-shaped single-crystal W-doped VO_2 nanoparticles synthesized through a one-step hydrothermal reaction. (i) Transmission electron microscopy (TEM) image of a VO_2 nanorod and the corresponding SAED pattern (inset). (j) TEM image and the SAED pattern (inset) of the VO_2 powders

produced through the hydrothermal method at 260 °C for 8 h. The nanobump is indicated by the red circle. (k) Schematic illustration of the evolution of Sb-doped VO_2 nanoparticles. (l and m) TEM images of the VO_2 nanocrystals produced through the hydrothermal method at 260 °C for 12 h with 3% (l) and 40% (m) Sb^{3+} addition, respectively. Insets of (l) and (m) show the corresponding calculated size distributions. Figures reproduced with permission from: **a-c**, ref.[130], American Chemical Society; **d**, ref.[140], Elsevier; **e**, ref.[124], Elsevier; **f**, ref.[131], Wiley; **g-h**, ref.[125], American Chemical Society; **i**, ref.[126], Elsevier; **j**, ref.[127], Elsevier; **k**, ref.[144], Royal Society of Chemistry.

3.2 Nanocomposites based on VO_2 crystals

3.2.1 Simulation

In the continuous VO_2 thin films, the thickness needs to be increased to overcome the insufficient ΔT_{sol}, but at the cost of depressing the T_{lum}.[146] A promising way to tackle the trade-off between ΔT_{sol} and T_{lum} is by fabricating nanothermochromic composite, which can be achieved by embedding VO_2-based nanoparticles in a dielectric matrix. The reported simulated and experimental results concerning VO_2-based nanocomposites are summarized in Table 3.

This concept was first developed by Li *et al.*, who demonstrated *via* calculations based on effective medium theory (EMT) that a system composed of well-dispersed VO_2 nanoparticles (reflective index of ε_p) in a dielectric host has advantages over continuous thin films.[147,148] Dilute composites composed of three types of VO_2 nanoparticles (spheres, ellipsoids, and core-shell) embedded in a dielectric matrix were considered (Figure 6a-c) and the aspect ratio m is defined as a/c to describe the spheroidal geometry in the calculation. The selected refractive index of the matrix (ε_m) was similar to that of glass or a polymer. The composite thickness was set to 5 μm with a filling factor f of 0.01, which means that the effective thickness (including the VO_2 nanoparticles) is 0.05 μm, identical to one of the conditions calculated for the continuous films. They demonstrated than an increase in the aspect ratio leads to the higher $T(\lambda)$. Moreover, the highest $T(\lambda)$ for randomly oriented particles occurs when m = 1, *i.e.*, when the particles have a spherical shape. Compared with continuous thin films (T_{lum} = 38% at the same effective thickness), the T_{lum} for spheres (m = 1) increased to ~72% and ~62% for the insulating and metallic states, respectively. Meanwhile, for spheroids, the ΔT_{sol} between the two phases is ~20%, while it is only ~7% for continuous films. For the core-shell structure (Figure 6c), ε_c and ε_p denote the dielectric functions of the core (with diameter x) and the VO_2 shell (with thickness t), respectively.[148] Calculations were done by varying the refractive indexes of the core (n_c) and changing the ratio of x/t. $T(\lambda)$ was found to decrease with an increase in x/t. The adverse effect of a high x/t ratio on T_{lum} and T_{sol} becomes more pronounced with increasing n_c. The largest ΔT_{sol} was 20.9%, observed for hollow nanospheres (n_c = 1) with x/t = 10, which is superior to that of solid nanospheres (~16.7%). However, T_{lum} shows a concomitant decrease from 73.5% to 59%. Moreover, they demonstrated that inverted core-shell structures constructed by an outermost shell with a refractive index ranging from 0 to 2.5 surrounding a VO_2 core without remarkable enhancement of

thermochromic performance.

EMT does not consider light scattering by the nanoparticles, as the radii of the embedded nanoparticles are assumed to be substantially smaller than the wavelength, which is small enough to neglect light scattering. Hence, Laaksonen *et al.* further applied the four-flux method, a simplification of the multiple-scattering approach, together with EMT to determine the onset of light scattering.[149] In this approach, different fluxes in the forward and backward directions were collected to acquire the transmittance (direct and diffuse) and reflectance (specular and diffuse). The nanothermochromic properties of the VO_2-based nanocomposites were simulated for different-sized nanoparticles with radii of 5, 20, 50, and 100 nm.[149] The inference-free EMT showed good agreement with the four-flux theory when the radius of the embedded particles was less than 20 nm. As the nanoparticle size increased, the scattering was enhanced, and the difference between the four-flux theory and EMT became obvious. Such significant light scattering results in remarkable absorption and insufficient transmittance, which are not desired for applications of VO_2-based nanocomposites. Therefore, they concluded that VO_2 particles with sizes below or approximately 20 nm and fine crystallinity are crucial for applying VO_2-based nanocomposite coatings in practice.

3.2.2 Experiment

Non-responsive matrix

Over the past decade, many methods for preparing VO_2 nanoparticles with fine crystallinity have been explored and implemented, followed by dispersion in various host materials, for practical applications of nanothermochromics. These host materials are classified as non-responsive or responsive matrixes, depending on if they display distinct optical modulation during heating.

Polyurethane (PU) has been widely studied as a host material for VO_2-based thermochromic composites. The incorporation of pure VO_2 nanocrystals with PU was achieved by Chen *et al*., with excellent thermochromic properties observed.[150] Finely crystalline VO_2 nanoparticles with average diameters of 26 nm were prepared *via* a hydrothermal method based on the burst-nucleation process induced by precursor decomposition at a critical temperature. Through the assistance of polyvinylpyrrolidone (PVP), VO_2 nanoparticles were well dispersed in a PU matrix to form a visible homogenous film. The composite displayed a much lower reflectance (below 8%) than the pure VO_2 coating on bare glass. The low reflectance, combined

with the small size and high crystallinity of the VO_2 nanoparticles, revealed a remarkable ΔT_{sol} of 22% and an acceptable T_{lum} of 45.6% at low temperature and 40.0% at high temperature, which is very close to the highest simulation results (ΔT_{sol} = 23.7%). Shen *et al.* used a solid-state reaction to form aggregations of spherical VO_2 nanoparticles with a τ_c in the range of 43.5 to 59.3 °C.[151] The reduction of τ_c may be due to the presence of an amorphous VO_2 phase surrounding the crystallized phases. However, their best-performing composite only showed a ΔT_{sol} of 9%. Gao *et al.* introduced the VO_2-PU composite to Sb-doped SnO_2 (ATO), a typical material that can largely block transmittance in the infrared (IR) range while maintaining high transparency.[152] By optimizing the experiment, the ATO-VO_2-PU composite achieved comparable ΔT_{sol} and T_{lum} to the VO_2-PU foil without ATO. They further tested their applied properties in two model houses and demonstrated that the addition of ATO filler made the composite more effective at shielding IR transmittance than the VO_2-PU composite.

Embedding doped VO_2 nanoparticles into the PU matrix also achieved superior nanothermochromic properties. The primary reason for doping other elements into VO_2 nanoparticles is to reduce the τ_c from ~70 °C to around room temperature. Upon substituting V atoms with F,[71] Mg,[66] W or Zr atoms,[103] both VO_2(M) and VO_2(R) lattice structures are distorted due to structural defects induced by the dopants. Upon increasing the doping level, the structural difference between the high-temperature and low-temperature states decreases, which in turn, leads to the reduction of the MST latent energy, therefore resulting in a decrease in the τ_c. An increase in dopant concentration usually deteriorates the solar modulation performance due to the appearance of lattice defects and morphological changes in the nanoparticles. In addition to Mg and W+Zr dopants, T_{lum} can be fairly maintained by F doping or slightly increased by introducing Zr into the VO_2 lattice. Among the dopants, F and W able to lower the τ_c to a comfortable temperature of 35 and 29 °C, respectively, but large reduction in τ_c requires a high doping level at the cost of weakening the thermochromic performance. Although Ti doping fails to reduce τ_c, 1.1 at% Ti achieves the simultaneous improvement of T_{lum} (from 46% undoped to 53%) and ΔT_{sol} (from 13% undoped to 17%).[72] However, further increasing the Ti doping level does not further benefit the thermochromic properties. Dopant of Ti not only affects the thermochromic properties of VO_2 nanoparticles but also modifies the color of VO_2-based nanocomposite foils, as it widens the band gap of VO_2, inducing a

blueshift in the absorption spectrum that lightens the original brownish-yellow color to a faded yellow color.

The motivation for employing core-shell structures is to protect VO_2 nanoparticles from oxidation and maintain the outstanding nanothermochromic properties. The SiO_2 shell can act as a protective layer to restrain oxygen diffusion and prevent thermodynamically unstable VO_2 from being oxidized. Gao *et al.* successfully prepared VO_2-SiO_2 core-shell nanocrystals and integrated them in a PU matrix to produce flexible thermochromic foils.[153] The fabrication process is described in Figure 6d. VO_2 nanoparticles were sequentially treated by PVP and tetraethyl orthosilicate (TEOS) to obtain silica shells. To promote the dispersion of the core-shell structures in PU, they were further treated with a trace amount of silane coupler. The composite was cast on a polyethylene terephthalate (PET) substrate. As shown in Figure 6e-f, the films with high (Sample I) and low (Sample II) VO_2 content display excellent flexibility. Jin's group further explored core-shell structures by producing VO_2@SiO_2 nanorod structures or introducing W-doped VO_2-SiO_2 core-shell nanoparticles.[154,155] Both methods achieved decent performance, including high solar modulation and luminous transmittance, as well as improved stability. They suggested that the thermochromic performance benefited from surface plasmon resonance (SPR) and calculated the tunable SPR position by varying the filling factor and aspect ratio of the VO_2@SiO_2 nanorod structure. When 3 at% W is doped into VO_2 nanoparticles with SiO_2 shells to ensure excellent weatherability, the resulting $V_xW_{1-x}O_2$@SiO_2 nanocomposites, with their near-room-temperature transition, can achieve a T_{lum} of 49% and ΔT_{sol} of 15%. They noted that based on four-flux theory, a small particle size (~ 20 nm), good crystallinity, and good dispersion of nanocrystals in the composite are essential to achieve outstanding nanothermochromic properties. Ji *et al.* synthesized the VO_2@ZnS core-shell nanoparticles through the homogeneous precipitation method, finding that the VO_2 nanoparticle in the center exhibited tunable emissivity in the mid-wavelength and long-wavelength thermal atmospheric windows, wheras the ZnS shell, as an infrared transparent material, not only modified the color of VO_2 nanoparticle, but also enhanced the oxidation resistance.[156]

Alternatively, Long's group adopted a transparent Si-Al gel as the host material. They utilized mechanical attrition (bead-milling) to obtain VO_2 nanoparticles without using a heating source.[157] The nanoparticles were well dispersed in the Si-Al gel and then coated on glass. An optimized thermochromic performance was achieved with a

3 μm-thick film containing 10 wt% VO_2. Following this work, the Si-Al gel/VO_2 composite was further developed to various micropatterned structures *via* a facile screen-printing method.[158] By optimizing the size of the mesh opening, the VO_2 load, and the film thickness, they demonstrated that the micropatterned structures simultaneously improved the ΔT_{sol} (8.8%) and T_{lum} (67%) over those of continuous films (ΔT_{sol} of 6.9% and T_{lum} of 60%) and the best preformed film has ΔT_{sol} of 14.9% combined with T_{lum} of 43.3%, An elastomeric matrix of polydimethylsiloxane (PDMS) was employed by Moot *et al.* to incorporate 10-200 nm VO_2 nanoparticles into stretchable composite films,[159] In addition, the film thickness could be easily reduced by stretching the films, which induces the formation of voids at the high-stress area and thus facilitates a significant enhancement in the T_{lum} from 45.6 to 55.4% as well as a slight increase in the IR modulation from 7.6 to 8.1% (due to the blueshift of the plasmon resonance spectral position).

Inorganic host materials, such as TiO_2, were explored by Gao's group.[160] They successfully fabricated inorganic-inorganic composite coatings by the two-step annealing of VO_2 nanoparticles in TiO_2 sol. In addition to acceptable thermochromic effects, these coatings showed additional advantages of self-cleaning, low contact angle and photocatalytic decomposition of organic contaminants. These functions introduced by the TiO_2 matrix improved the weatherability of VO_2-based smart windows.

Responsive matrix

Though numerous advancements in VO_2-based non-responsive composites have improved the thermochromic performance, the best T_{sol} is still below 30%, which is limited by the spectral range that VO_2 can modulate. Solar energy is dense in the visible range, but VO_2 cannot regulate in this region due to the limited difference of the optical constants in spectrum range of 400 to 800 nm between its rutile and monoclinic phases. Incorporating a thermoresponsive host material with VO_2 has been proven to be a promising way to overcome this limitation.

Recently, Zhou *et al.* applied a thermoresponsive matrix to a VO_2-based composite for solar energy modulation.[161,162] Pure poly-N-isopropylacrylamide (PNIPAm) is transparent below the lower critical solution temperature (LCST) and becomes translucent when the temperature increases, accompanied by a change in the NIR transmittance. In this research, phase separation of the PNIPAm hydrogel

controlled the luminous modulation, while the phase transition of VO_2 nanoparticles contributed to the NIR modulation, providing an extremely high ΔT_{sol} of 35% and a high average T_{lum} of 60%. Figure 6g illustrates the formation of the laminated VO_2/hydrogel hybrid thin film and the mechanism to regulate the solar energy at different temperature. Compared with pure hydrogel of the same thickness, the VO_2/PNIPAm hybrid thin film had a slightly lower T_{lum} at both 20 and 90 °C due to the introduction of the VO_2 nanoparticles, but the IR modulation ability was dramatically increased, which lead to the high ΔT_{sol}. The large contrast in the hybrid structure occurred in both the visible and NIR range, leading to a high solar modulation which is difficult to be reached by the non-responsive matrix. Later, Yang *et al*. developed a hydrogel based on hydroxypropyl cellulose (HPC).[163] Similar to PNIPAm, HPC becomes translucent during heating due to its LCST behavior. In addition to excellent thermochromic performance (ΔT_{sol} of 36.0% and T_{lum} of 56%), the prepared composite displayed a suitable τ_c of approximately 50 °C by adjusting the τ_c of W-doped VO_2 nanoparticles and HPC. They suggested that the small liquid pores and aggregated polymeric blocks at elevated temperature could scatter the incident visible light and become translucent or opaque above the LCST.

In a different work, Jin's group combined VO_2 nanoparticles with a thermochromic ionic liquid, which typically increases the absorbance during heating over the range of 650 to 750 nm rather than over the whole visible range as the hydrogel does.[164] In the experiment, an ionic liquid-nickel-chlorine (IL-Ni-Cl) complex was observed to undergo a gradual color change from colorless to blue during heating. The VO_2/IL-Ni-Cl composite demonstrated outstanding optical regulation properties (ΔT_{sol} of 26.5%) and maintained good transparency (T_{lum} of 50%). More interestingly, the films exhibited a distinct color change from brown at 20 °C to green at 80 °C, which was believed to be a synergistic effect of the color variations in pure VO_2 and pure IL-Ni-Cl films (Figure 6h). This method provides an alternative way to simultaneously improve the unfavorable brownish-yellow color of VO_2 and achieve good solar energy modulation. They then applied similar methods to cobalt(II)- and nickel(II)-based ligand exchange thermochromic systems (CLETS and NCLETS[165,166]and similar results were obtained.

Table 3 Summary of experimental and simulation results of VO_2-based thermochromic nanocomposites.

Category	Matrix		Embedded nanocrystals		T_{lum} (%)	ΔT_{sol} (%)	τ_c	Ref.
			Types	Dopant \ structures				
Simulation	Non-responsive	\	spheroidal VO_2 particles		67.0	20.0	\	[147]
		\	VO_2-based core-shell structures		59.0	20.9	\	[148]
Experiment	Non-responsive	PU	VO_2		45.6	22.3	—	[150]
			VO_2 and Sb-doped SnO_2		51.4	11.7	\	[152]
			Doped VO_2	F	48.7	10.7	↓	[71]
				Mg	54.2	10.6	↓	[66]
				Zr	60.4	14.1	↓	[103]
				W+Zr	56.4	12.3	↓	[103]
				W	56.0	12.7	↓	[150]
				Ti	53.0	17.2	—	[72]
			Core-shell structure	VO_2-@-SiO_2	27.8	13.6	—	[153,154]
				$V_xW_{1-x}O_2$-@-SiO_2	50.6	14.7	↓	[155]
		Si-Al gel	VO_2		59.1	12.0	—	[157]
		PDMS	VO_2		85	\	—	[159]
		TiO_2	VO_2		61.2	14.6	—	[160]
	Responsive	PNIPAm	VO_2		62.6	34.7	↓	[161,162]
		HPC	Doped VO_2	W	56.0	36.0	↓	[163]
		IL-Ni-Cl	VO_2		55.2	26.5	\	[164]
		CLETS	VO_2		59.2	20.8	\	[165]
		NLETS	VO_2		71.0	18.2	\	[166]

Note: "—" means unchanged; "↓" means decrease; "\" means data not available; "PNIPAm" means poly(N-isopropylacrylamide); "HPC" means hydroxypropyl cellulose; "CLETS" means Co-based ligand exchange thermochromic system; "IL-Ni-CL" means liquid-nickel-chlorine complex; "NLETS" means nickel-based ligand exchange thermochromic system.

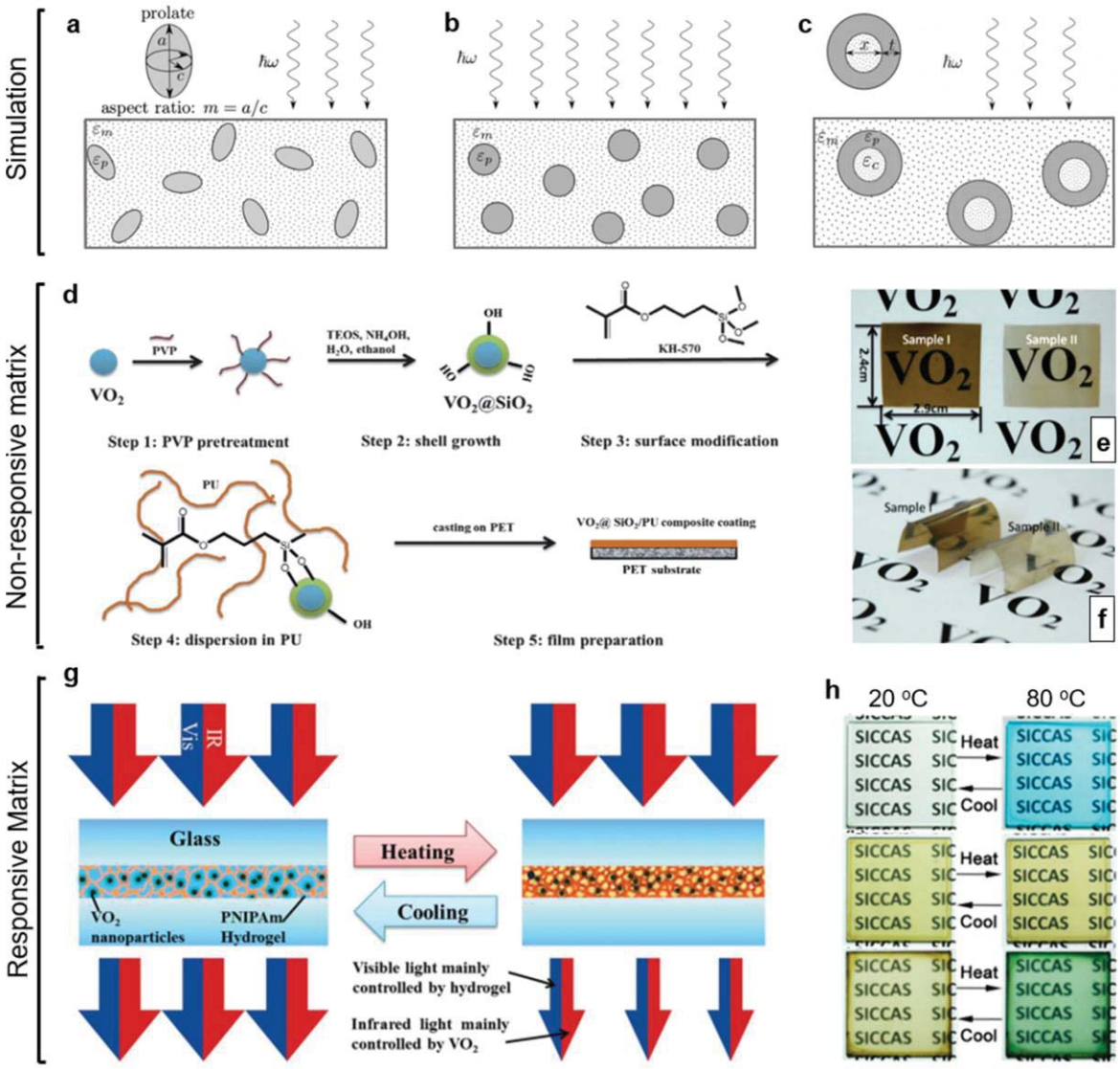

Figure 6. Nanocomposites based on VO_2 crystals to enhance the thermochromic properties. (a-c) Structural models of composites embedded with nanocrystals having three different nanostructures: (a) ellipsoids, (b) spheres, and (c) core-shell nanoparticles. The dielectric functions of the matrix, nanoparticle, and core in the core-shell structure are denoted ε_m, ε_p, and ε_c, respectively. The aspect ratio is defined as m = a/c for ellipsoids and spheres (m = 1). The *x* and *t* indicate the core diameter and the shell thickness, respectively. The incident light is characterized as $h\omega$. (d) Scheme of the preparation procedure for the VO_2@SiO_2/PU composite, starting from VO_2 nanoparticles. (e,f) Photographs of flexible thermochromic films based on VO_2@SiO_2/PU composites with high (Sample I) and low (Sample II) VO_2 contents. (g) Illustration of the solar modulation behavior of the VO_2/PNIPAm-based composites. Both the visible and infrared light transmittance decreased when the films were heated. (h) Photographs of the films based on the pure IL-Ni-Cl complex (top row), VO_2 nanoparticles (medium row), and VO_2/IL-Ni-CL composite (medium row) at 20 (left column) and 80 °C (right column), respectively. The IL-Ni-Cl complex and VO_2/IL-Ni-CL composite have distinct temperature-responsive color changes. Figures reproduced with permission from: **a-b**, ref.[147], American Institute of Physics; **c**, ref.[148], American Institute of Physics; **d-f**, ref.[153], Royal Society of Chemistry; **g**, ref.[162], Royal Society of Chemistry; **h**, ref.[164], American Chemical Society.

3.3 Porous VO_2 films

The introduction of air-filled nanopores, which are considered to be a secondary component in VO_2 films, has been proven to be an effective method to improve the thermochromic performance, especially the T_{lum}. Gao *et al.* calculated the spectral transmittance of a nanoporous VO_2 film on a fused-silica-glass substrate with variable porosity and thickness by employing the optical-admittance recursive method, which is based on the optical-admittance function.[167-170] Based on the calculation, they plotted a useful diagram that correlates the thermochromic performance, including ΔT_{sol} and visible transmittance of porous VO_2 films at low temperature ($T_{lum,low}$), with the thickness and porosity of the film (Figure 7a). An optimizing thermochromic performance is demonstrated up to a ΔT_{sol} of 20% with a $T_{lum,low}$ of 45%. They suggested that ΔT_{sol} could be enhanced without a decrease in $T_{lum,low}$ because of the depression of the porosity-derived reflection. The progress of simulation and experimental of porous VO_2 films are summarized in Table 4.

Incorporating removable additives into the vanadium precursor has been demonstrated to be a facile way to fabricate porous VO_2 films. Gao *et al.* pioneered the porous films and successfully produced nanoporous thermochromic VO_2 films by a polymer-assisted deposition method.[171] The pores in the final films are formed from PVP degradation and shrinkage of the gel films during high-temperature annealing (Figure 7b). These air-filled pores had feature sizes much smaller than the visible wavelength lower the low optical constants (Figure 7c), resulting in a high luminous transmittance, T_{lum} = 43.3%, and solar modulation, ΔT_{sol} = 14.1%. A micro/nanosized (20-50 μm/100-500 μm) hierarchical porous structure was developed by Huang *et al.* through the self-assembly of cetyltrimethylammonium vanadate (CTAV), which exhibited largely enhanced visible-light transmittance.[172] Later, surfactants such as cetyltrimethyl ammonium bromide (CTAB),[61] polyethylene glycol (PEG),[173] and sodium dodecyl sulfate (SDS)[174] were reported to successfully serve as nanostructure-directing agents for VO_2 films.

Instead of incorporating removable additives into the precursor, Long's group achieved porous VO_2 films by controlling the drying procedure *via* a lyophilization method (freeze-drying).[175] In their experiment, the sols were frozen at low temperature and pressure, and then, the solvent was removed *via* sublimation. This procedure can easily circumvent the collapsed pores induced by evaporation under

atmospheric pressure. This group further explored the effect of gas effect during annealing.[176] When a CO_2 atmosphere was applied during sintering, nanoporous VO_2 films were formed, and the crystallization temperature of VO_2 was reduced to 550 °C from 750 °C when sintering in vacuum.

A spontaneous self-templating and assembly process during dual-phase transformation was successfully applied by Liu *et al.* to prepare porous VO_2 structures.[177] In the experiment, an aqueous vanadium precursor including vanadyl dichloride (VCl_2), hydrazine (N_2H_4), hydrochloric acid (HCl), and PVP was spin-coated on a quartz substrate and then dried under nitrogen (Figure 7d). The formation of hydrous colloids was promoted by N_2H_4 but impeded by HCl. During the evaporation process, the promotional effect of N_2H_4 was enhanced, but the quenching effect of HCl weakened, forming hydrous colloidal spheres from the homogeneous precursor. These spheres self-assembled into a close-packed structure at the colloid-substrate interface when saturation was reached in the hydrous colloids (Figure 7e). After that, the hollow sphere structures developed at 300 °C and then collapsed and crystallized to VO_2 during annealing at 500 °C (Figure 7f-g). These processes have been demonstrated experimentally (Figure 7h-k). By optimizing the experimental conditions, a high transmission (95.4% at 700 nm) was achieved, accompanied by ΔT_{sol} = 5.5%, for a honeycomb VO_2 film with a thickness of 65 nm. In contrast to the self-assembly relying on dual-phase transformation, Zhang *et al.* prepared self-assembled VO_2 nanonets on a (001) single-crystal sapphire substrate by synchronously controlling the growth direction and crystallographic orientation.[178] The key is the lattice-matching between the low-surface-energy plane of VO_2 and the 3-fold symmetric (001) plane of sapphire, which induced the growth of (020) VO_2 on the (001) sapphire substrate followed by the growth of (001) VO_2 to suspended nanorods in three equivalent directions. The films were produced on the wafer scale and displayed dramatic fatigue endurance.

Table 4 Summary of porous VO_2 films

Category	Preparation method		Structure	Pore size	ΔT_{sol} (%)	T_{lum} (%)	Ref.
Simulation	\		Random porosity	Nano	20	45	171
Experiment	Incorporating removable additive	PVP	\	Nano	14.1	43.3	171
		CTAV	Hierarchical porous structure	Nano/ micro	\	46.5	172
		CTAB	\	Nano	\	\	61
		PEG	\	Nano	\	\	173
		SDS	\	Nano	\	\	174
	Process control	Freeze-drying	\	Nano	14.7	50.0	175
		Sintering in CO_2 atmosphere	\	Nano	2.2	35.9	176
	Self-assembly	Dual-phase transformation	Quasi-honeycomb	Nano	5.5	\	177
		Crystallographic orientation control	Interconnected nanonet	Nano	\	\	178

Note: " \ " means data not available.

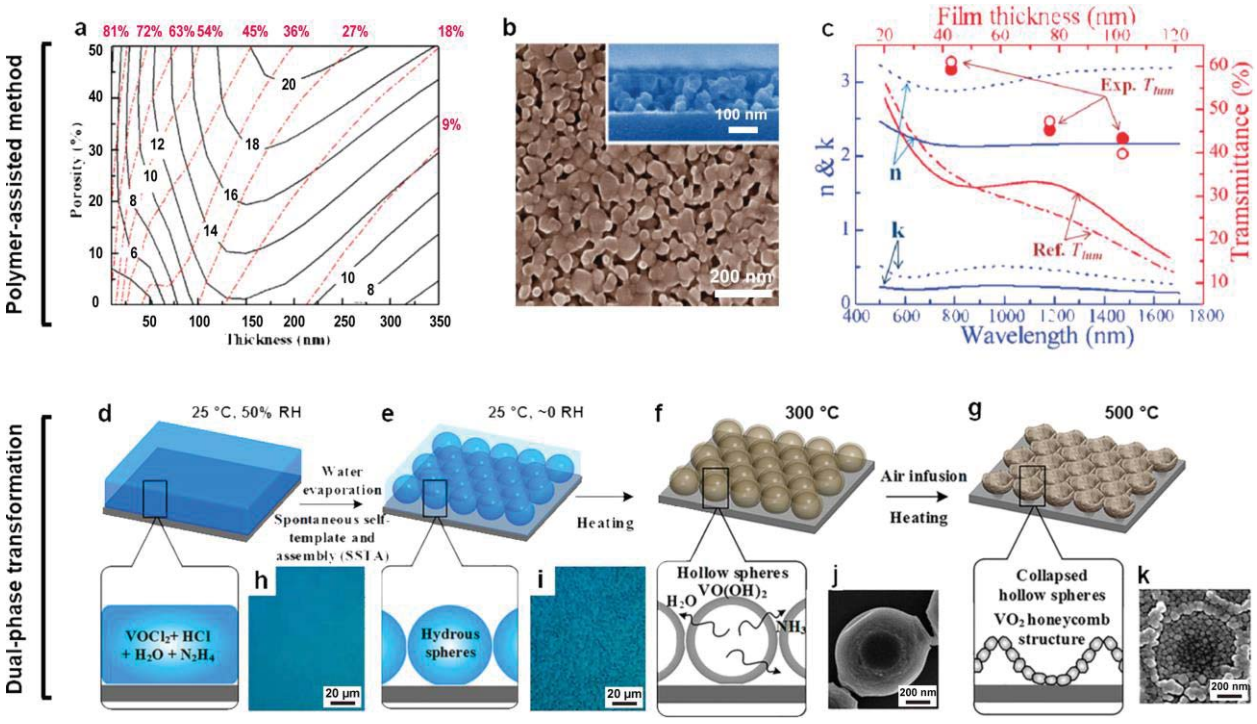

Figure 7. Porous VO_2 films to enhance the thermochromic properties. (a) Summary of the calculated thermochromic performance as a function of porosity and film thickness. $T_{lum,low}$ (visible transmittance of the porous VO_2 film at low temperature) and ΔT_{sol} are denoted by the red dotted lines and black solid lines, respectively. (b) The porous morphology of a 147 nm-think VO_2 film, as an example, from the top and side view (inset). (c) Optical properties of porous VO_2 films comparing with reference (non-porous VO_2 film). The optical constants (n and k) in experiment and reference are indicated as the solid and dotted blue lines. Experimental T_{lum} is recorded at 20

(solid sphere) and 90 (open circle) ºC. The reference of T_{lum} at 20 (solid red line) and 90 (dashed red line) ºC are presented. (d-k) Schematic of the self-templating and assembly during the dual-phase transformation process, which includes four steps: (d) deposition of a homogeneous solution-based precursor on a substrate, (e) assembly of self-templated hydrous sphere arrays, (f) formation of hollow $VO(OH)_3$ spheres, and (g) formation of the honeycomb-nanostructured VO_2 film *via* the collapse of hollow spheres. (h) and (i) are the corresponding photographs of steps (d) and (e), respectively. (j) and (k) are the SEM images presented as demonstrations of steps (f) and (g), respectively. Figures reproduced with permission from: **a-c**, ref.[171], American Chemical Society; **d-k**, ref.[177], American Chemical Society.

3.4 Grid VO_2 films

Films based on grid-structured VO_2 have attracted increasing interest due to the great potential of structure-induced thermochromic enhancements, including but not limited to increased transmittance, antireflection, and localized surface plasmon resonance (LSPR). Previous studies, including simulation and experimental works, are summarized and classified in Table 5.

The group of Long demonstrated that nanogrid structure is able to significantly enhance the T_{lum} without deteriorating ΔT_{sol} and demonstrated by 3D finite difference time domain (FDTD) method to numerically optimize a number of parameters, including structural models, cavity size, periodicity, film thickness, and fill factor.[179] In the simulation, three structural models are calculated：square holes in square lattices，circular holes in square lattices, and circular holes in hexagonal arrangement (Figure 8a). The thermochromic performance of square holes in square lattices is summarized in Figure 8b. Moreover, a competitive thermochromic performance (T_{lum} = 76.5% and ΔT_{sol} = 14.0%) was demonstrated on hexagonal-packed circular cells of VO_2 with a radius of 80 nm, periodicity of 160 nm, and thickness of 300 nm.

Grid VO_2 films with periodicity in microscale are processable and the same group has applied the electrodeposition method to successfully assemble the VO_2 NPs to electrodes by tuning the ionic strength (Figure 8c).[180] Flexible thermochromic film was produced by depositing the VO_2 NPs on to grid Cu/PET substrates, in which the NPs assembled alone the grid Cu electrodes (Figure 8d). An optimized ΔT_{sol} of 13.9% and T_{lum} of 38.4% were demonstrated. Another facile method, the mesh printing method was reported by Lu *et al.* to prepare micropatterned VO_2/Si-Al gel composites by mounting a mesh above a glass substrate with controllable distance (Figure 8e).[158] Films *via* the method display competitive performance which up to a ΔT_{sol} of 14.9% under a T_{lum} of 43.3%. These two fabrication methods are facile, efficient, and controllable.

Preparation of grid films with periodicxity in nanoscale is challenging. The colloidal nanolithography method was developed as a facile and productive method to prepare patterned nanostructures.[181] Xie's group applied monolayer colloidal crystal (MCC) templates made of polystyrene (PS) nanospheres to prepare periodic porous VO_2 films.[182] In their study, MCC templates consisted of closed-packed polystyrene nanospheres were sequentially immersed vanadium precursor, then removed during

annealing to leave the VO_2 nanonet structures. Ke *et al.* modified the nanosphere lithography method and produced diverse patterned VO_2 films with tunable periodicity and nanostructures, including nanoparticle, nanonet, and nanodome arrays.[183] The fabrication process is flexible by controlling the plasma etching (PE) duration and precursor viscosity, illustrating as the synthetic routes in Figure 8f. When a short PE duration is applied, nanoparticle and nanodome arrays can be produced using low-viscosity (Route 1) and high-viscosity (Route 2) precursors, respectively. Nanonet arrays can be fabricated by prolonging the PE duration and using low-viscosity precursors (Route 3). The produced 2D patterned VO_2 arrays are highly uniform (Figure 8g). The patterned VO_2 films were further explored in thermochromic smart window and demonstrated an optimizing performance of ΔT_{sol} = 13.2% and T_{lum} = 46%. For the first time, hexagonally patterned VO_2 nanoparticle arrays with average diameters down to 60 nm and a periodicity of 160 nm were fabricated on the centimeter scale. Interestingly, such structure gives rise to tunable peak positions and intensities of the LSPR at different temperatures. The LSPR was also found to redshift with an increase in the particle size and the reflective index of the media, and these results fit well with the trend calculated using the 3D FDTD method.

Table 5 Summary of grid-structured VO_2 films.

Category	Preparation method	Structure	ΔT_{sol} (%)	T_{lum} (%)	Ref.
Simulation	\	Grid	14.0	76.5	179
		Nanoparticle array	\	\	183
Experiment	Electrodeposition	Micro-grid	13.9	38.4	180
	Mesh printing	Micro-patterned	14.9	43.3	158
	Nanosphere lithography	Nanonet	7.9	\	182
		Nanonet	\	\	183
	Modified nanosphere lithography	Nanoparticle array	13.2	46.0	183
		Nanodome array	\	\	183

Note: " \ " means data not available.

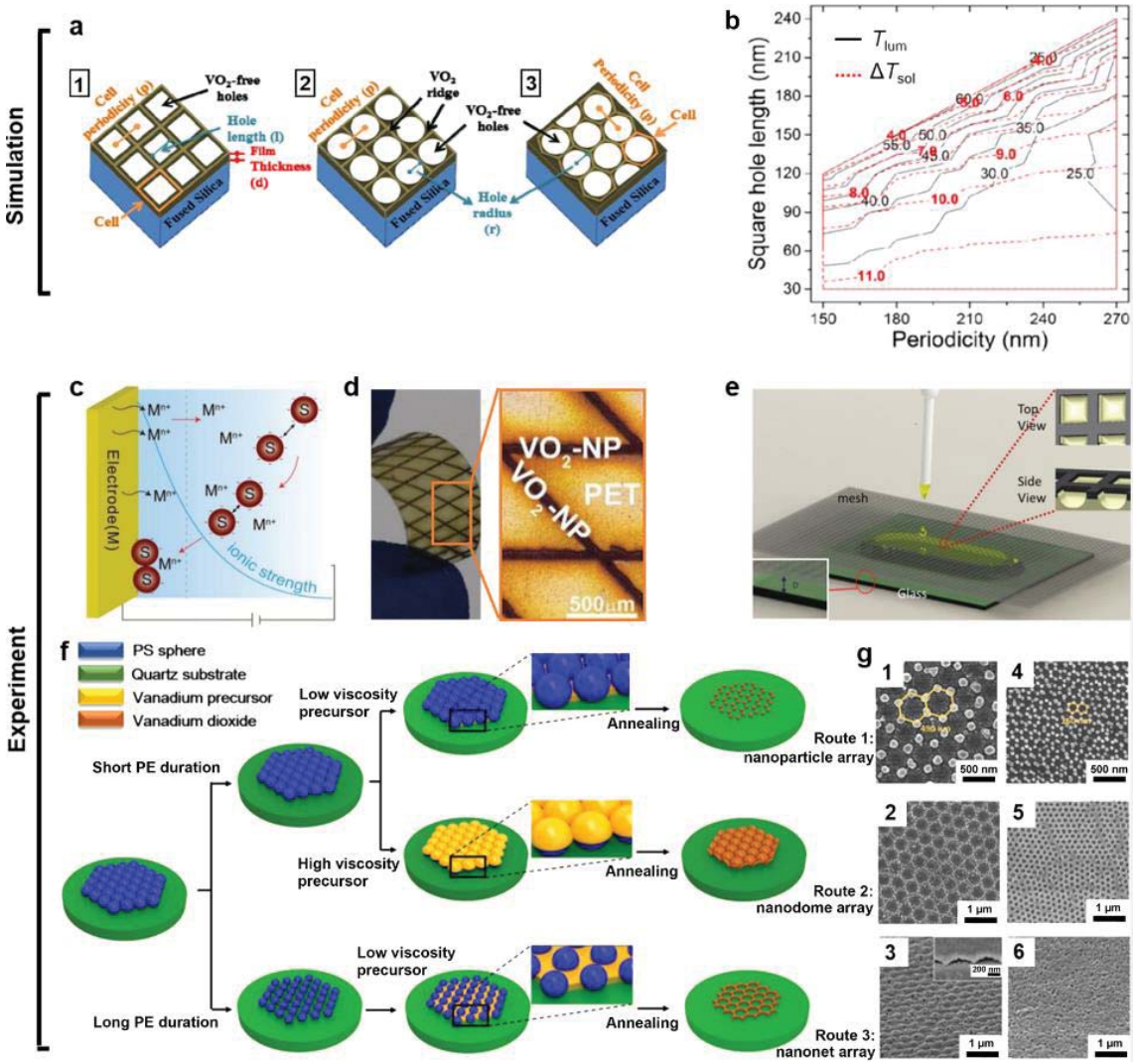

Figure 8. Films based on grid-structured VO_2 to enhance the thermochromic performace. (a) Simulation models of the grid films with square holes (a1) and circular holes (a2) in square lattices as well as the circular holes in hexagonal arrangement (a3). (b) Summary of the calculated T_{lum} and ΔT_{sol} of the model with square holes in square lattice under various periodicity and square hole length. (c) Schematic of the electrodeposition process based on ionic strength. The metal ions (M^{n+}) can reduce the interparticle repulsion among substances (S) and facilitate the S deposition. (d) Photograph of the sample which contains VO_2 NPs deposited on flexible grid Cu/PET film (left) and the optical microscopy image of the grid structure (right). (e) Illustration of the mesh printing method, in which the thickness of sample is controlled by the distance (*D*) between the glass substrate and the mesh mounted above. (f) Process of the template-assisted method for patterned VO_2 nanocrystals. Three types of the 2D periodic VO_2 nanocrystals, namely, nanoparticle, nanonet, and nanodome arrays, are derived from the nanosphere MCC by controlling the PE duration and the precursor viscosity through routes 1-3 in (f). (g) SEM images of periodic nanoparticle, nanonet, and nanodome VO_2 arrays with periodicities of 490 nm (g1-g3) and 160 nm (g4-g6). (g3) and (g6) are the tilted-view SEM images. The periodicity can also be controlled to be the same as the nanosphere diameter of the MCC templates. Figures reproduced with permission from: **a,b,** ref.[179], The Optical Society; **c,d,** ref.[180], Royal Society of Chemistry; **e**, ref.[158],Royal Society of Chemistry; **f,g**, ref.[183], American Chemical Society.

3.5 Biomimetic VO_2 patterning

The usual properties of biomimetic structures have attracted great research interest, especially in light manipulation and the design of high-performance optics.[184] Recently, the integration of a bioinspired artificial surface with VO_2-based thermochromic smart windows was shown to have great potential through the simultaneous enhancement of ΔT_{sol} and T_{lum} as well as the efficient modification of the unfavorable brownish-yellow color of VO_2.

Moth-eye nanostructures can efficiently eliminate reflection because the sub-wavelength nipple array generates a continuous refractive index gradient between the air and the medium, effectively reducing the refractive index gap at the air-medium interface (Figure 9a-b).[185,186] Taylor *et al.* introduced the moth-eye structures to thermochromic VO_2-based intelligent glazing.[187] In their simulation, the VO_2-coated nipple arrays were designed to be hexagonal-close-packed (HCP) on a glass substrate (Figure 9c). The thermochromic performances were calculated by numerically optimizing these dimensions using the 3D FDTD method and are plotted in Figure 9d. As shown in Figure 9d, structures with heights lower than 500 nm are preferred, as these structures are reflective, especially in visible and dense solar energy regions. A decent thermochromic performance of T_{lum} = 59.9% combined with ΔT_{sol} = 19.4% was revealed at point C in Figure 9d. VO_2 films with moth-eye structures were successfully prepared by Qian *et al.* by coating VO_2 onto fused silica substrates with moth-eye structures that were pre-fabricated *via* nanosphere lithography (Figure 9e-f).[188] The periodicity of the prepared films was precisely controlled to range from 210 to 1000 nm. They found that the T_{lum} increases with decreasing periodicity, and moreover, the sample with a periodicity of 210 nm simultaneously enhanced T_{lum} and ΔT_{sol} over those of the planar sample. Future research can be directed at reducing the periodicity, which may be a challenge for the fabrication of sub-100 nm patterns.

The opalescent or iridescent colors commonly observed in butterflies,[188] flora,[186] *etc.* are produced by “photonic crystals”, a concept first proposed in the 1980s (Figure 9g-h).[189] Photonic crystals are composed of periodically structured materials, generating a photonic band gap (PBG) and distinct structural colors by the coherent diffraction of visible light.[190] Ke *et al.* applied photonic crystals to VO_2-based smart windows to successfully modulate the unfavorable brownish-yellow color commonly observed for VO_2 films.[191] They prepared 2D HCP SiO_2-VO_2 core-shell structures on

glass substrates with a fixed shell thickness of 20 nm (Figure 9i). As demonstrated by FDTD simulation, thermochromic films relaying on such photonic structures display statically diameter-dependent modulation in the visible range, while maintaining good thermochromic performance (up to T_{lum} = 49.6% and ΔT_{sol} = 11.0%) (Figure 9j). The PBG-induced transmittance peaks and troughs were further verified experimentally with a variation in diameter, and structure-induced colors were observed to change from yellow-brown to red, blue, or green. However, the optimized ΔT_{sol} is limited to 3.1% in the experiment, much lower than the simulated result (11.0%). This difference is mainly attributed to the sol-gel method employed in the experiment, which resulted in half-coated spheres (Figure 9k-l) rather than perfect core-shell structures. The coating uniformity could be improved by using vapor deposition methods with different core materials and assembly.

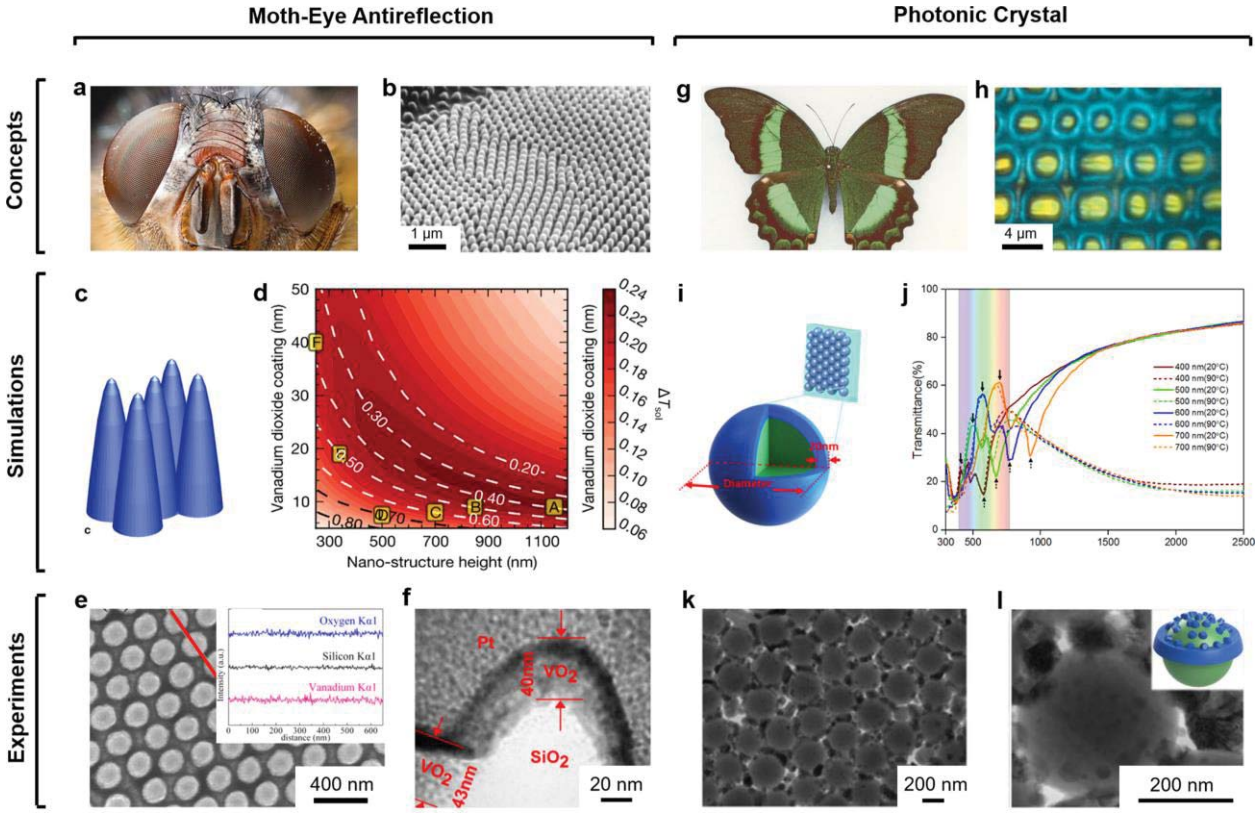

Figure 9. Integration of a bioinspired artificial surface to enhance the thermochromic performace. (a) Photograph of the compound eyes of Calliphora. (b) The antireflection structures on the surface of its ommatidium. (c) Three-dimensional illustration of the VO_2-coated nipple arrays used in the simulation and (d) the calculated ΔT_{sol} map based on the FDTD parameter search. (e) Produced moth-eye nanostructured VO_2 films containing (f) the individual nipple structure of VO_2-coated silica. (g) Photograph of a butterfly and (h) the two distinct structure-induced colors simultaneously appearing on its wings. (i) Three-dimensional illustration of the 2D

SiO_2-VO_2 core-shell photonic crystals used in the simulation and (j) the calculated transmittance spectra with diameters ranging from 400 to 700 nm at 20 and 90 °C. (k-l) TEM images of the produced 2D HCP SiO_2-VO_2 core-shell photonic crystals under low and high magnification. Inset of (l) is the illustration of an individual photonic crystal. Figures reproduced with permission from: **b**, ref.[186], Nature Publishing Group; **c-d**, ref.[187], The Optical Society; g-h, ref.[186], Nature Publishing Group; **i-l**, ref.[191], American Chemical Society.

3.6 Multifunctional antireflection coating

Challenges remain in the development of VO_2-based smart windows. A major issue is the low T_{lum} attributed to the strong reflection and absorption in the visible-light region (λ = 380-760 nm).[2] Antireflection coatings (ARCs) have been proved to be one of the effective strategies for enhancing the low T_{lum} in the visible region without degrading the thermochromic properties of the VO_2 films.[29,31] In addition, integrations with other cutting-edge glazing techniques can introduce some practical functions that are unable to be achieved by pure VO_2 films, such as anti-oxidation,[192] hydrophobicity[193] and photocatalysis.[194]

The selection of ARC relies on the light interference between thin-film interfaces, which is determined by the optical constants and thicknesses of the ARC.[195] The refractive index (RI) of VO_2 is around 2.8 in the visible-light region (λ = 380-760 nm).[196] For a VO_2 film with a thickness of 50 nm, the highest enhancement in T_{lum} occurs when the thickness of the ARC is approximately 55 nm and the RI is approximately 2.2, as shown in Figure 10a.[197] According to this proposed refractive index criterion,[197] a variety of materials are potential candidates for the ARCs, such as TiO_2,[198] ZrO_2,[197] CeO_2[199] and SnO_2.[200] Table 6 summarizes the T_{lum} and ΔT_{sol} of several VO_2-based multilayers before and after the application of an ARC.

For the VO_2-based double-layered films, TiO_2 is commonly selected as the ARC due to its refractive index of 2.2.[197] For instance, in the TiO_2(40 nm)/VO_2(50 nm) double-layered structure designed by Jin *et al.*, the thicknesses of the TiO_2 and VO_2 layers were optimized by calculation to improve the T_{lum} of the TiO_2/VO_2 double-layer structure (from 30% to 49%) (Figure 10b-c).[198] Xu *et al*. fabricated a ZrO_2(56 nm)/VO_2(50 nm) double-layer structure by sputter deposition, in which the ZrO_2 layer acted as the ARC, showing that the T_{lum} was improved (from 32.3% to 50.5%).[197] Koo *et al*. prepared a CeO_2(60 nm)/VO_2(39 nm) double-layered structure, where the CeO_2 layer acted as the ARC due to its high refractive index (2.3) and high transparency to visible as well as near-infrared light.[199] The sample exhibited an obviously enhanced T_{lum} (from 40.0% to 67.5%), and the CeO_2 layer also acted as an anti-oxidation layer for the VO_2 layer.[199]

For the VO_2-based multilayered films, Jin *et al.* reported a TiO_2/VO_2/TiO_2 triple-layered structure with an elevated T_{lum} (from 30.9% to 57.6%) (Figure 10d-e).[201] However, this VO_2-based multilayered film exhibited a low ΔT_{sol} of 2.9%. This intrinsically low ΔT_{sol} (<16%) is due to the fact that VO_2 has a higher RI from

500 to 2200 nm wavelength below its τ_c, which causes excessive reflection at a lower temperature. Liu *et al.* designed an RI-tunable ARC coating to improve the antireflection effect at a lower temperature, thereby maximizing ΔT_{sol} for various VO_2 nanosubstrates, such as the continuous thin films, nanocomposites, and periodic micro-patterning films.[202] The best performing coatings could maximize ΔT_{sol} (from 15.7% to 18.9%) and increase T_{lum} (from 39% to 44%) simultaneously.[202] Chen *et al*. conducted a simulation to optimize the thickness of each layer in the $VO_2/TiO_2/SiO_2$ multilayers and then developed an all-solution method to fabricate the double-layered film consisting of a TiO_2 antireflection layer on a planar VO_2 film.[203] Their results showed that T_{lum} was enhanced from 40.3% to 61.5% and could be further enhanced to 84.8%, moreover, the value of ΔT_{sol} could be improved to 15.1%, which is much higher than the value of the single VO_2 films of 10%.[203] Other designs have also been reported, for instance, Mlyuka *et al*. prepared a $TiO_2/VO_2/TiO_2/VO_2/TiO_2$ five-layered structure with T_{lum} increased by 4% (from 41% to 45%) (Figure 10f).[204] However, the optical performances of structures with more than five layers have not been extensively investigated, probably due to the difficulties in both optical design and process control.

Some unique properties, such as anti-oxidation,[205,206] hydrophobicity[188,193] and self-cleaning,[207] have been recently introduced by designing VO_2-based multilayered structures. For instance, Liu *et al*. prepared a Si-Al-based ARC with greatly enhanced T_{lum} (from 51.0% to 62.3%), hydrophobicity (contact angle of 111°) (Figure 10g), and anti-oxidation protections.[193] Zheng *et al*. reported a large-scale (400×400 mm^2) TiO_2(A)/VO_2(M)/TiO_2(R) multilayered film that presented at least three functions, antifogging/self-cleaning, thermochromic, and antireflective properties attributed to the top TiO_2(A), the middle VO_2(M), and the bottom TiO_2(R) layers, respectively (Figure 10h-j).[207]

Thermal emissivity is another important property of VO_2-based smart windows. A high value of thermal emissivity implies that there is an intensive energy exchange between the window surface and its surroundings through thermal radiation and absorption, which weakens the thermal insulating ability of the window. To achieve smart functionality, a VO_2-based window should have suitable transmittance to control of heat gain as well as low emissivity to modulate the heat loss. In cold weather, the heat flux is from indoors to outdoors, therefore a smart window should have high transmittance of heat from sunshine, as well as low emissivity to prevent

the heat loss from indoors to outdoors. In hot weather, the direction of heat flux is opposite, from outdoors to indoors, therefore a smart window should transmit less possible IR light, as well as have low emissivity to prevent the heat flow from outdoors to indoors.

The thermal emissivity is 0.59 and 0.83 for typical VO_2(R) and VO_2(M) films (thickness of 68 nm), respectively.[208] This high emissivity indicates the strong ability of the VO_2-based windows to exchange energy with its surroundings through thermal radiation processes. Recently, a number of papers have concerned the combination of the thermochromic properties of VO_2 and the low emissivity, in which transparent conductive oxides such as F-doped SnO_2 (FTO)[200] and Al-doped ZnO (AZO)[205] or noble metals (Ag[209] and Pt[210]) with low emissivity have been incorporated into VO_2-based multilayered films. Table 7 summarizes the emissivity of the VO_2 based multilayered structures. For instance, Zhang *et al*. deposited VO_2 thin films on FTO glasses substrates (Figure 10k), and then incorporated a TiO_2 ARC on the VO_2 thin films to form a TiO_2/VO_2/FTO three-layered structure, which boosted the T_{lum} (from 34% to 44%) and elevated the reflectance in the infrared region while retaining the low-emissivity performance of the original VO_2/FTO double-layered structure (from 0.13 to 0.24) (Figure 10l-m).[200] Kang *et al*. prepared $SiO_2/Pt/VO_2$ multilayered films, in which the Pt layer depressed the emissivity (from 0.85 to 0.56 for VO_2(M), and from 0.84 to 0.53 for VO_2(R)), and the SiO_2 layer acted as an ARC to enhance the T_{lum} (from 25.1% to 37.9%).[210]

Table 6 The T_{lum} and ΔT_{sol} before and after the application of antireflection coatings (ARC) in different multilayered structures.

Layered Structure	ARC	T_{lum} (%) (without ARC)	T_{lum} (%) (with ARC)	ΔT_{sol} (%) (without ARC)	ΔT_{sol} (%) (with ARC)	Ref.
TiO_2/VO_2	TiO_2	32	49	4.4	7.0	[198]
ZrO_2/VO_2	ZrO_2	32.3	50.5	\	\	[197]
CeO_2/VO_2	CeO_2	40	67.5	5.2	5.4	[199]
TEOS/VO_2	TEOS	47.3	52.7	13.6	16.4	[202]
Si-Al /VO_2/ITO	Si-Al	51.0	62.3	3.4	4.0	[193]

$TiO_2/VO_2/TiO_2$	TiO_2	30.9	57.6	3.9	2.9	201
$TiO_2/VO_2/SiO_2$	TiO_2	40.3	61.5	7.4	6.9	203
TiO_2/VO_2/FTO	TiO_2	34	44	4.4	8.8	200
$SiO_2/Pt/VO_2$	SiO_2	25.1	37.9	\	\	210

Note: " \ " means data not available

Table 7 The emissivity (ε_T) of VO_2 based multilayered structures.

Layered Structure	ε_T of VO_2(R)	ε_T of VO_2(M)	Thickness of VO_2	Ref.
VO_2 single layer	0.59	0.83	68 nm	[208]
TiO_2/VO_2/FTO	0.24	0.13	55 nm	[200]
VO_2/FTO	0.27	0.19	65 nm	[200]
VO_2(W and Zn doped)/FTO	0.33	0.20	/	[211]
VO_2/SiO_2/Au	0.71	0.22	30 nm	[212]
AZO/VO_2	0.31	0.32	40 nm	[205]
Pt/VO_2	0.53	0.56	40 nm	[210]

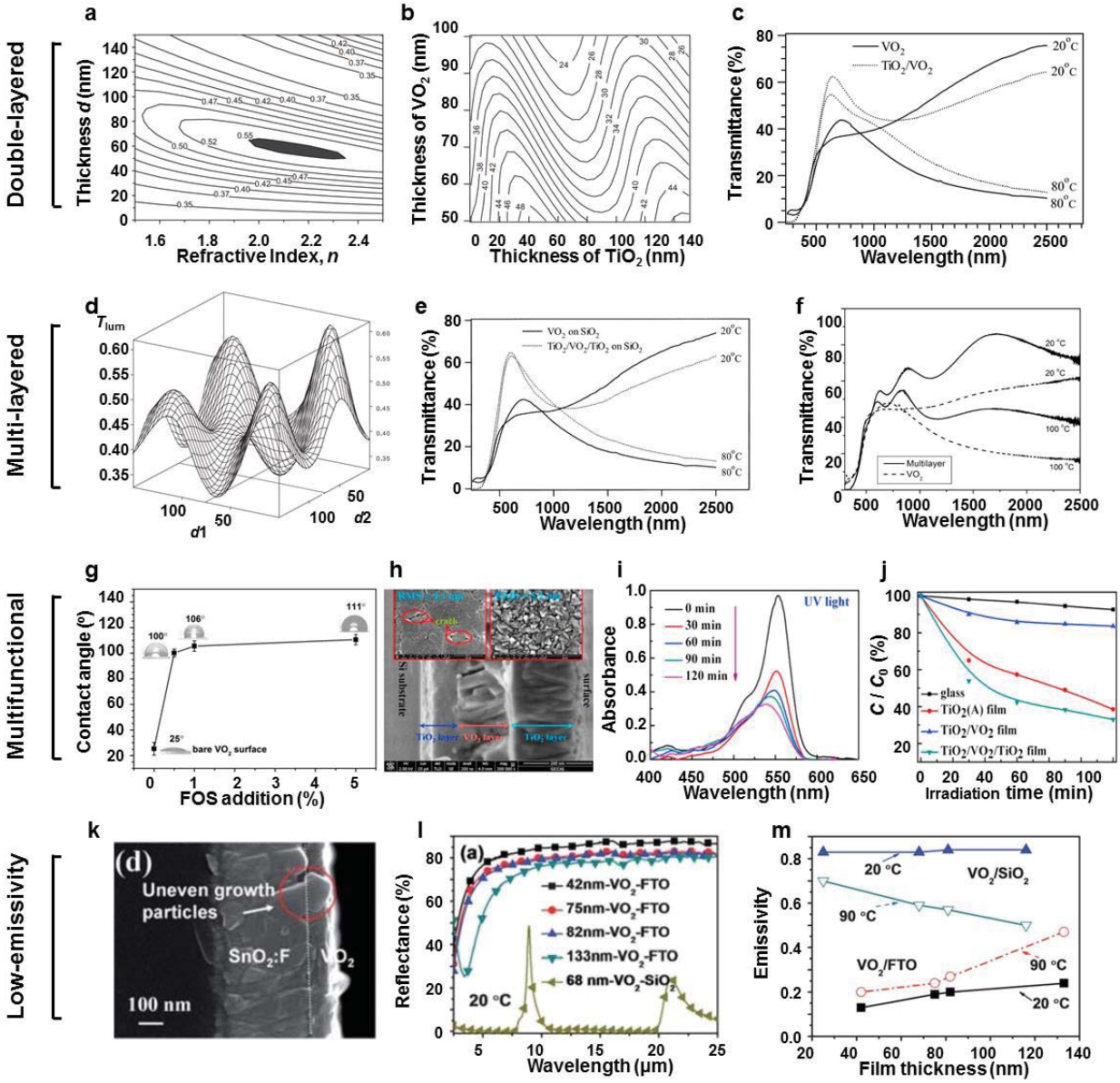

Figure 10. Multifunctional antireflection coating to enhance the thermochromic performace of VO_2. (a) The effects of the refractive index n and thickness d of the ARC on the T_{lum} of planar 50 nm VO_2 films. The optimized n and d are presented as the dark area on the contour map. (b) The thickness effect on the T_{lum} of TiO_2 and VO_2 on fused silica glass substrates. (c) Respective transmittance spectra of 50 nm VO_2 films with or without an ARC (40 nm of TiO_2) at 20 and 80 °C. (d) Calculated T_{lum} of the $TiO_2/VO_2/TiO_2$ layered structure, $d1$ and $d2$ are the thicknesses of the top and bottom TiO_2 layers, respectively. (e) Transmittance spectra of a TiO_2 (20 nm)/VO_2 (50 nm)/TiO_2 (25 nm) sandwich structure at 20 and 80 °C. (f) Transmittance spectra of a $TiO_2/VO_2/TiO_2/VO_2/TiO_2$ multilayer film at 20 and 100 °C. The results of the VO_2 films in (e) and (f) represent control samples. (g) The effect of fluorooctyl triethoxysilane (FOS) addition on the contact angle on the VO_2 surface. (h) Cross-sectional FESEM image of the multilayer film (the insets are the surface morphology of VO_2(M) (left) and TiO_2(A) layers (right), respectively). (i) Time-resolved absorption spectra of a rhodamine B (RhB) solution, which indicates the gradual degradation of RhB on the multilayer film. (j) Photodegradation of RhB solution over the films (TiO_2(A), TiO_2(R)/VO_2(M), and TiO_2(R)/VO_2(M)/TiO_2(A))

under UV light (C_0 and C represent the initial and real-time concentration of RhB during the irradiation test). (k) The cross-sectional FESEM image of a VO_2 film on a FTO (F-doped SnO_2) substrate. (l) Thickness-dependent reflectance spectra of the VO_2 film on a FTO substrates at 20 °C. The sample with a SiO_2 substrate is a reference. (m) Thickness-dependent emissivity of the VO_2 film on a FTO substrate. Figures reproduced with permission from: **a**, ref.[197], Elsevier; **b-c**, ref.[198], IOPscience; **d-f**, ref.[201], Elsevier; **g**, ref.[193], Elsevier; **h-j**, ref.[207], Elsevier, **k-m**, ref.[200], Royal Society of Chemistry.

4. Energy efficiency

Practical energy conservation is the ultimate purpose of developing VO_2-based thermochromic layers, and researchers have been investigating this topic from both simulations and experimental aspects.

In the simulational studies, Saeli *et al*. firstly used energy-modelling studies to investigate the behavior of a series of VO_2 films and their associated energy consumptions (Figure 11a-b).[213,214] They compared three different VO_2 films, one is prepared *via* atmospheric pressure CVD, one is the commercial product (sputtered silver-coated glass or blue body-tinted glass), and another one is thermochromic films with "ideal" optical properties based on experimentally obtainable options. Their results indicated that the ideal coatings have a clear advantage in reducing energy consumption compared with the commercial products (Figure 11c), but the best performance of a real VO_2 film was observed for the sample with the lowest phase-transition temperature, which meant that the film was always in the metallic state. These results suggested that the heat reflecting and absorbing properties of the VO_2 layers contributed more strongly to their energy-conservation performance than their thermochromic nature. Increased absorption might present an advantage for the moth-eye class of smart window, because the window's temperature will be strongly influenced by the light intensity and not merely the temperature. This behavior could endow the window with additional photochromic properties.

In the experimental studies, building the model houses is the common strategy to estimate the energy efficiency of VO_2-based smart windows is. The VO_2-based layers are coated onto the flat glass and then fixed as windows or roofs for a model house. Blank glasses of the same size are used in another model house as a control experiment. Two infrared lamps are employed as the irradiation source and placed at a certain distance from the model houses. Two thermocouples are placed at the same position in the model houses to monitor temperature changes.

For instance, Gao's *et al*. prepared a single-layer VO_2 structure (30×40 cm^2) on glass using the polymer-assisted deposition method, and then built a model house to evaluate the optical properties of VO_2-based smart windows.[2] Their results indicated that under similar infrared irradiation, the temperature difference between the two inner rooms was approximately 9 °C(Figure 11d), suggesting that a significant amount of irradiation was blocked. Chang *et al.* recently developed a sandwich structure of $Cr_2O_3/VO_2/SiO_2$ multilayers.[215] For quantitative characterization of their practical

energy conservation, two pieces of flat glass (75×75 mm^2) coated with $Cr_2O_3/VO_2/SiO_2$ multilayer were roofed for a model house.[215] The results showed that the temperature in the model house with blank glass was increased by 84.8%, wherea the temperature of house with $Cr_2O_3/VO_2/SiO_2$ coated glass was only increased by 29.8% (Figure 11e). The infrared thermal imaging demonstrated that after 6 min of irradiation, the glass coated by $Cr_2O_3/VO_2/SiO_2$ structure shows a pink hue indicating high thermal emissivity. On the contrary, relatively low thermal emissivity has been shown by the laurel green hue of the blank glass (Figure 11f). Kim *et al.* prepared a graphene-supported VO_2 flexible film, and then fabricated a model house with VO_2/graphene/PET windows to measure the inner-house temperature changes (Figure 11g-h).[216] The results showed that the temperature difference between two inner rooms (graphene/PET and VO_2/graphene/PET) was about 5.8 °C (Figure 11i), indicating that a significant amount of irradiation was blocked by the graphene/VO_2 window.

Ye, Yang and Gao *et al*. evaluated the energy-saving efficiency of VO_2 layers in both theoretical simulations and experiments.[217,218] The VO_2 layers used in the experiments were VO_2 nanocomposite foils provided by Gao *et. al*. The researchers constructed a 2.9×1.8×1.8 m^3 low-mass room with a window size of 1.65 × 1.65 m^2 (Figure 11j-k). The results measured by Yang *et al*. indicated that the room equipped with the VO_2 foils experienced a 10.2-19.9 % savings in cumulative cooling load compared with the room equipped with ordinary glazing. The extension of this observed performance to a conventional residential room in the hot-summer and warm-winter zone was simulated using BuildingEnergy (simulation software developed by Ye *et al.*). The simulated results indicated that the use of the VO_2 glazing could yield a ~9.4% savings in electricity consumption (Figure 11l).

Ye *et. al* have conducted a series of comprehensive investigations on the energy savings performance of VO_2-based smart windows.[219-221] They found that not all VO_2 glazings are "'smart" due to the absorption of the coatings and concluded that the VO_2 glazing tends to exhibit smart regulation capacities if it experiences a high decrease in solar transmittance and a low increase in solar absorptivity after the VO_2 changes into its metallic state. In their other work of evaluating the energy saving performance of materials and components in passive buildings, the results showed that a representative VO_2 glazing is "energy-saving" in summer but is "energy-wasting" in winter due to its low solar transmittance. These studies reveal the importance of the

transmittance and absorption of VO_2 film/coatings in practical energy-saving efficiency and provide a direction for the development of VO_2-based smart windows.

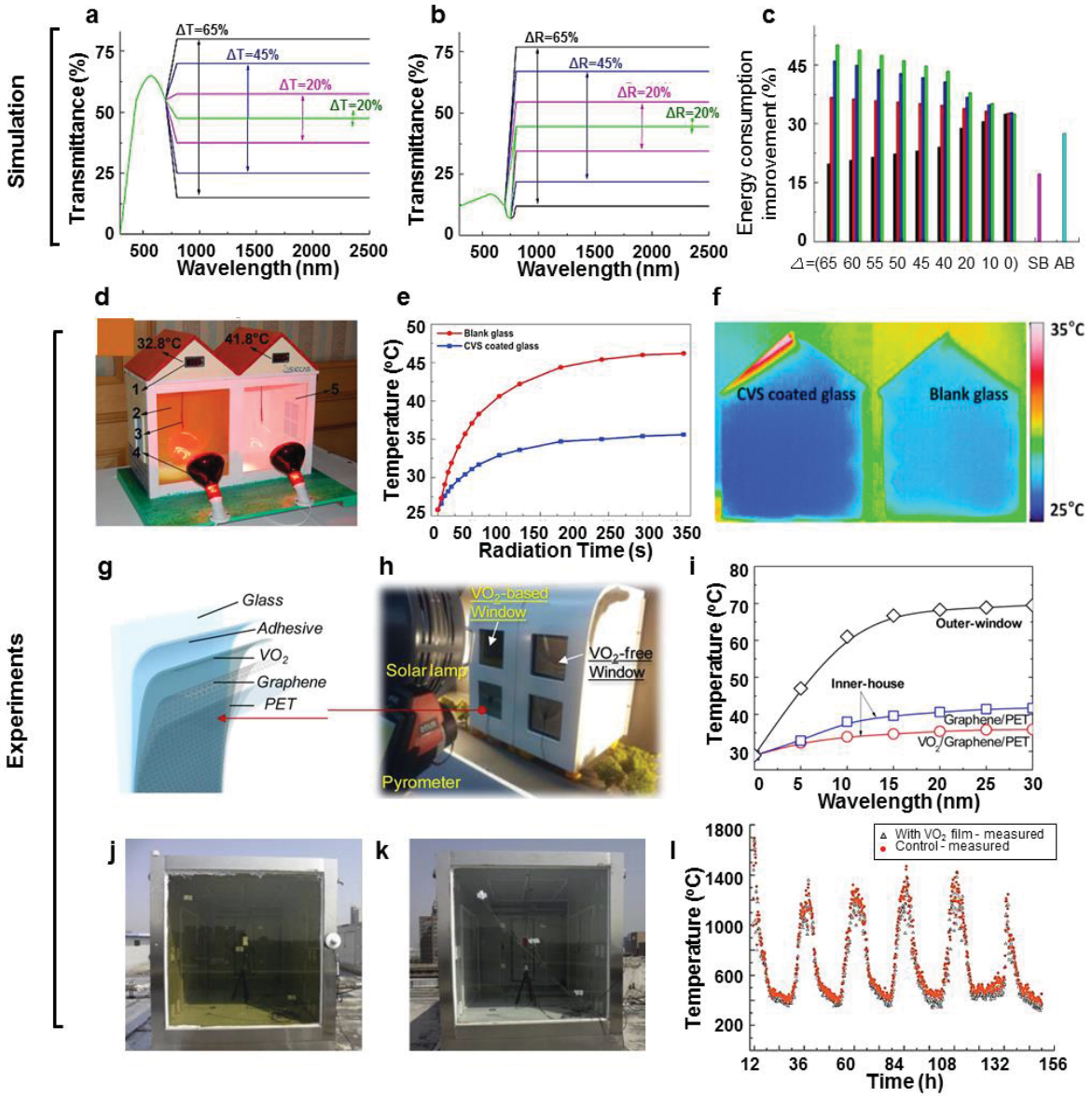

Figure 11. (a)Transmittance and (b) reflectance spectra for ideal thermochromic coatings, demonstrating cold-hot decreases of 65%, 45%, 20% or 0% and energy-consumption improvement (c) for ideal thermochromic films with various changes in transmittance and reflectance. Black: phase-transition temperature is 35 °C, red: 30 °C, blue: 25 °C, green: 20 °C, SB: sputtered silver-coated glass, AB: blue body-tinted glass. (d) Photograph of a model house (1, temperature monitor; 2, VO_2 glass; 3, temperature probe; 4, infrared lamp; 5, blank float glass). (e) Temperature curve inside the model house with $Cr_2O_3/VO_2/SiO_2$ coated glass (blue line) and blank glass (red line). (f) Infrared thermal images of the model house with $Cr_2O_3/VO_2/SiO_2$ coated glass and blank glass. (g) Structure of the graphene-supported VO_2 film. (h) Photograph of model house equipped with VO_2-based (VO_2/graphene/PET film) and VO_2-free window (graphene/PET film). (i) Temperature change of model house upon solar irradiation as a function of exposure time. (j) Photographs of Room A with VO_2 foils and (j) Room B with ordinary glazing. (l) Variations in the simulated cooling

load (Aug. 1st to Aug. 7th, 2013). Figures reproduced with permission from: a-c, ref.[214] Elsevier; Figures reproduced with permission from: d, ref.[2] Elsevier; Figures reproduced with permission from: e-f, ref.[215] Elsevier;Figures reproduced with permission from: g-i, ref.[216]American Chemical Society; Figures reproduced with permission from: j-l, ref.[222] Elsevier.

5. Conclusions and perspectives

In conclusion, smart windows represent an important technology for increasing indoor comfort and reducing electrical consumption in the automotive and building sectors. We summarized the progress in VO_2-based thermochromic smart windows in Figure 12 by classifying different categories and distinguishing the simulation and experiment results in terms of τ_c, ΔT_{sol} and T_{lum}. Thermochromic windows are highly promising for constant T_{lum}, and smart regulation of indoor solar transmission automatically based on their achieved transmittance-modulation ranges together with the relatively simple structure, facile fabrication and low cost. Although the ΔT_{sol} of VO_2 is lower than that of a gasochromic and electrochromic window, but it can be further improved by integrating with responsive matrix and morphology engineering. Hence, VO_2 smart windows are an important category in energy saving smart windows' applications. Indeed, flexible VO_2 foils fabricated by dispersing VO_2 nanoparticles into a matrix and coating of this VO_2-incorporated matrix onto a polymer substrate have been produced on the industrial scale.

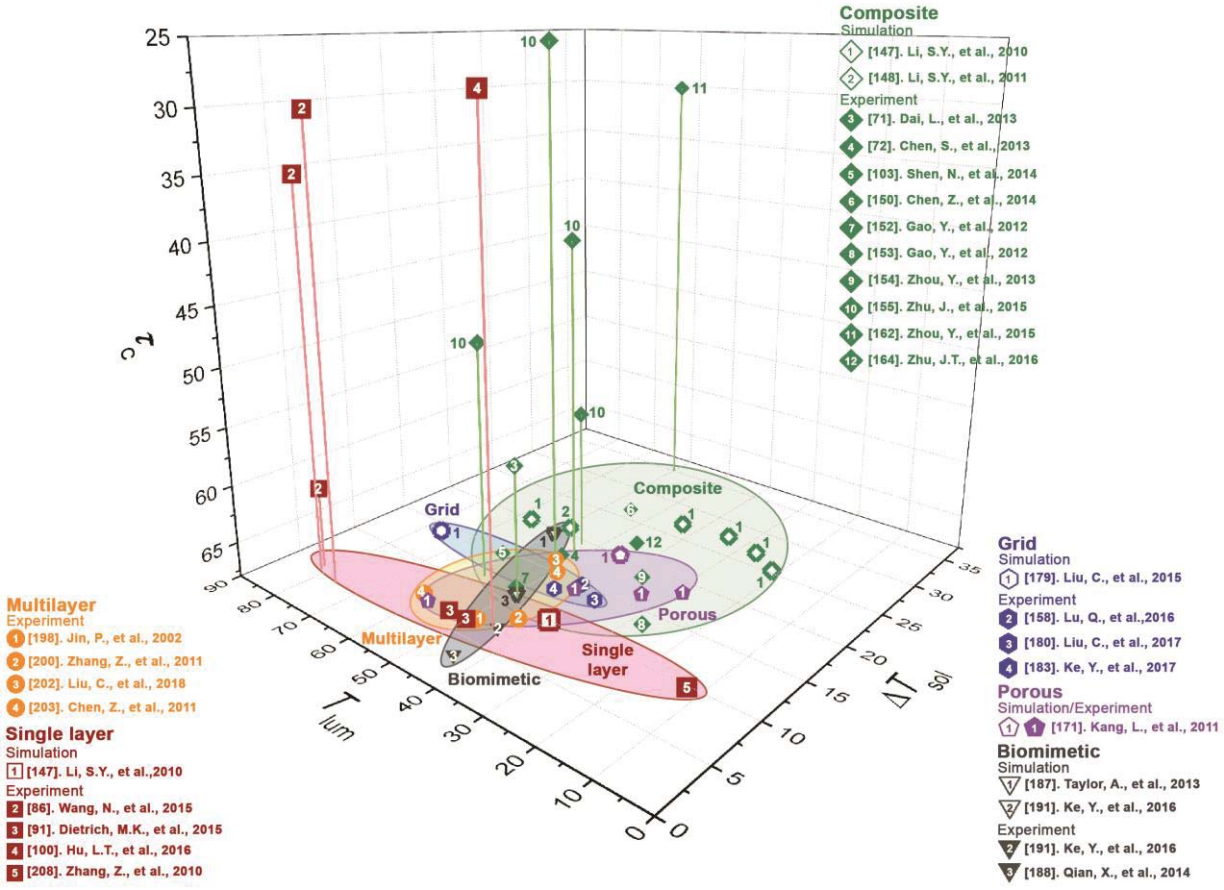

Figure 12. Summary of thermochromic performance (τ_c, ΔT_{sol}, and T_{lum}) in some of the best reported and selected works.

The application of VO_2 thermochromic smart windows is promising and just beginning. Some problems still needed to be addressed to further widen their applications.

A balance between transition temperature, visible transmittance and solar modulation ability. Based on recent studies, the simultaneous reduction of τ_c, enhancement of ΔT_{sol} and T_{lum} is rather difficult, as shown in Figure 12. Low VO_2 loading are generally favorable for increasing the T_{lum}, but jeopardizing ΔT_{sol}. Doping is undoubtedly an effective strategy to decrease the τ_c, but the other two parameters are typically degraded as well. Currently doping is limited in continuous films and nanocomposites (Figure 12); more investigation can be extended to other categories such as biomimetic, gridding, controlled porosity and multilayered structure engineering. For the practical applications, more dopants and co- or multi- doping need to be examined in atomic level *via* the combination of simulations and experiments together with more structure designs in nano or micro level.

It is worth mention that IR blocking in warm weather is an important aspect for energy-saving applications of thermochromic materials. For comparison, commercial low-emission glass with the application of three Ag layers can reach 90% blockage while VO_2 in state-of-art designs can reach less than 70%. The ΔT_{sol} is another important index of energy saving which can hardly even reach up to 30%. To facilitate the commercialization of VO_2 films, ideally the IR blockage and ΔT_{sol} should be largely increased to 90% and 50% respectively. However, this is a veritable challenge.

Color. Due to its strong absorption, VO_2 typically demonstrates a brownish-yellow color. The color has limited effects on the visible transmittance, and color preference is closely related to cultural background. Generally, a colorless coating or coloration with light gray/blue is most favorable (at least in China). In some areas of Southeastern Asia or Arabia, a golden color is more favorable. In this case, the brownish-yellow color of VO_2 would be acceptable. However, certain modifications are still required to tune the color. Although some simulations have suggested that doping may be an effective strategy to alter the color by shifting the adsorption edges, experimental results have shown that only limited changes can be achieved. Complexion with dyes or responsive matrix, either organic or inorganic, can modulate the original color of VO_2 at the expense of the ΔT_{sol} and T_{lum} of VO_2 films or transparency, which may not be a good solution in some applications. Structural coloration has been proved effective to change its color but some degradation of the

thermochromic performance and the complicated fabrication approach need to be investigated further. To address this concern, more creative ideas are needed.

Emissivity. Solar heating results from the near-IR region of the solar spectrum, whereas blackbody emissivity of room temperature objects occurs in the mid-IR regions. The former contributes to heat gains from the sun, while the latter is an important way to transmit heat from hot side to cold side. To achieve smart energy-saving functionality, a coating should have switchable transmittance to control of heat gain from sun as well as low emissivity to restrict the heat exchanging between indoors and outdoors. VO_2 films, especially those porous films synthesized by solution-based process, usually demonstrate emissivity as large as 0.83, which is much larger than that of double-layered silver-based low-emission glass (0.3-0.4). This implies that glass coated with only VO_2 layers performs poorly in the management of environmental heat. Using a double-layered film composed of VO_2 and a layer of noble metals or transparent conductive oxides can decrease the emissivity, accompanying unfavorably with a large decrease in the ΔT_{sol}. To resolve this problem, some new structures and/or material systems together with more fundamental studies of should be developed and integrated with VO_2.

Stability. As a transition metal, vanadium is multi-valance element, which exhibits +3, +4, +5 and mixed valences. VO_2(M) can be oxidized to vanadium oxides or their hydroxides, especially in the presence of moisture. This instability results in serious durability problems in practical applications. One solution involves the formation of VO_2 in an inert oxide shell, which is used to separate VO_2 from oxygen. This method has been certified to be useful to some degree, but the process to prepare a core-shell structure is not easy to control. Furthermore, this treatment step leads to the aggregation of well-dispersed nanoparticles, making them difficult to use. Increasing the crystallinity of VO_2 is also effective, but this method cannot completely address the problem.

Toxicity. The fate of nanoparticles in a variety of environmental and manufacturing settings has attracted immense attention and is a major obstacle for practical applications, especially in applications that have close contact with people and pets. Although some VO_2 products are commercially available (such as VO_2 foils in China), thorough research into the toxicological impact and possible hazards of VO_2 materials, especially in the form of nanoparticle, to human health and the environment is still in its infancy and is an urgent task to achieve large-scale

applications of VO_2. Addressing this issue seems more meaningful when considering that some vanadium oxides known today, for example V(V) and V(III), are toxic, although the toxicity of these oxides is closely related to their quantity. Therefore, collaboration studies should be done on the mechanisms at the cellular level, entry routes into the body and possible impacts to public health. In addition, the ways life cycle assessment (LCA) studies should be applied to analyze the toxicity of VO_2 nanoparticles.

Acknowledgments

This work is supported by Singapore Minster of Education (MOE) Academic Research Fund Tier one, RG124/16 and RG200/17, the National Research Foundation, Prime Minister's Office, Singapore under its Campus for Research Excellence and Technological Enterprise (CREATE) program, the National Natural Science Foundation of China (51325203 and 51402182), and the Outstanding Academic Leaders program of Shanghai Municipal Science and Technology Commission (15XD1501700).

Conflicts of interest

There are no conflicts to declare.

Author contributions

Y.C. and Y.K. contributed equally to this work. Y.C. wrote Section 2.1-2.3, 3.6, 4, and 5. Y.K. wrote Section 1, 3.1-3.5, and 5. Y.L. and Y.G. designed the framework of this manuscript and draft Section 1 and 5. C.L., Z.C., N.W., L.Z., Y.Z., and S.W. collected the data, participated in drawing the figures and examining the technical details. All authors read and approved the final manuscript.

Reference

1 Morin, F. J. (1959). Oxides which show a metal-to-insulator transition at the Neel temperature. Phys. Rev. Lett. 3, 34-36.

2 Gao, Y., Luo, H., Zhang, Z., Kang, L., Chen, Z., Du, J., Kanehira, M., and Cao, C. (2012). Nanoceramic VO_2 thermochromic smart glass: A review on progress in solution processing. Nano Energy 1, 221-246.

3 Ke, Y., Zhou, C., Zhou, Y., Wang, S., Chan, S. H., and Long, Y. (2018).

Emerging thermal−responsive materials and integrated techniques targeting the energy−efficient smart window application. Adv. Funct. Mater. 28, 1800113.

4 Cheng, Q., Paradis, S., Bui, T., and Almasri, M. (2010). Design of dual-band uncooled infrared microbolometer. IEEE Sens. J. 11, 167-175.

5 Zhu, H., Xiao, C., Cheng, H., Grote, F., Zhang, X., Yao, T., Li, Z., Wang, C., Wei, S., and Lei, Y. (2014). Magnetocaloric effects in a freestanding and flexible graphene-based superlattice synthesized with a spatially confined reaction. Nat. Commun. 5, 3960.

6 Yoon, H., Choi, M., Lim, T. W., Kwon, H., Ihm, K., Kim, J. K., Choi, S. Y., and Son, J. (2016). Reversible phase modulation and hydrogen storage in multivalent VO_2 epitaxial thin films. Nat. Mater. 15, 1113-1119.

7 Andersson, G., Paju, J., Lang, W., and Berndt, W. (1954). Studies on vanadium oxides. I. Phase analysis. Acta Chem. Scand. 8, 1599-1606.

8 Andersson, G., Parck, C., Ulfvarson, U., Stenhagen, E., and Thorell, B. (1956). Studies on vanadium oxides. II. The crystal structure of vanadium dioxide. Acta Chem. Scand. 10, 623-628.

9 Longo, J. M., and Kierkegaard, P. (1970). Studies on vanadium oxides. Acta Chem. Scand. 24, 420-426.

10 Haverkort, M. W., Hu, Z., Tanaka, A., Reichelt, W., Streltsov, S. V., Korotin, M. A., Anisimov, V. I., Hsieh, H. H., Lin, H. J., Chen, C. T., Khomskii, D. I., and Tjeng, L. H. (2005). Orbital-assisted metal-insulator transition in VO_2. Phys. Rev. Lett. 95, 196404.

11 Whittaker, L., Patridge, C. J., and Banerjee, S. (2011). Microscopic and nanoscale perspective of the metal-insulator phase transitions of VO_2: Some new twists to an old tale. J. Phys. Chem. Lett. 2, 745-758.

12 Belozerov, A. S., Korotin, M. A., Anisimov, V. I., and Poteryaev, A. I. (2012). Monoclinic M1 phase of VO_2: Mott-Hubbard versus band insulator. Phys. Rev. B 85, 276-279.

13 Goodenough, J. B. (1971). The two components of the crystallographic transition in VO_2. J. Solid State Chem. 3, 490-500.

14 Eyert, V. (2011). VO_2: A novel view from band theory. Phys. Rev. Lett. 107, 016401.

15 Petrov, G. I., Yakovlev, V. V., and Squier, J. (2002). Raman microscopy analysis

of phase transformation mechanisms in vanadium dioxide. Appl. Phys. Lett. 81, 1023-1025.

16 Ishida, H., Bihlmayer, G., and Liebsch, A. (2005). Coulomb correlations and orbital polarization in the metal-insulator transition of VO_2. Phys. Rev. B 71, 085109.

17 Rice, T. M., Launois, H., and Pouget, J. P. (1994). Comment on "VO_2: Peierls or Mott-Hubbard? A view from band theory". Phys. Rev. Lett. 73, 3042.

18 Wentzcovitch, R. M., Schulz, W. W., and Allen, P. B. (1994). VO_2: Peierls or Mott-Hubbard? A view from band theory. Phys. Rev. Lett. 72, 3389.

19 Dekorsy, T., Chong, H. H. W., Kieffer, J. C., Schoenlein, R. W., and Cavalleri, A. (2004). Evidence for a structurally-driven insulator-to-metal transition in VO_2: A view from the ultrafast timescale. Phys. Rev. B 70, 161102.

20 Cavalleri, A., Tóth, C., Siders, C. W., Squier, J. A., Ráksi, F., Forget, P., and Kieffer, J. C. (2001). Femtosecond structural dynamics in VO_2 during an ultrafast solid-solid phase transition. Phys. Rev. Lett. 87, 237401.

21 Rini, M., Chong, H. H. W., Fourmaux, S., Glover, T. E., Heimann, P. A., Kieffer, J. C., Schoenlein, R. W., and Cavalleri, A. (2005). Band-selective measurements of electron dynamics in VO_2 using femtosecond near-edge X-ray absorption. Phys. Rev. Lett. 95, 067405.

22 Baum, P., Yang, D. S., and Zewail, A. H. (2007). 4D visualization of transitional structures in phase transformations by electron diffraction. Science 318, 788.

23 Wei, J., Wang, Z. H., Chen, W., and Cobden, D. H. (2009). New aspects of the metal-insulator transition in single-domain vanadium dioxide nanobeams. Nat. Nanotechnol. 4, 420-424.

24 Yuan, X., Zhang, W., and Zhang, P. (2013). Hole-lattice coupling and photoinduced insulator-metal transition in VO_2. Phys. Rev. B 88, 035119.

25 Standard tables of reference solar spectral irradiances: Direct normal and hemispherical on a 37° tilted surface (2012). Active Standard ASTM G173, USA.

26 Lang, F., Wang, H., Zhang, S., Liu, J., and Yan, H. (2018). Review on variable emissivity materials and devices based on smart chromism. Int. J. Thermophys. 39, 6.

27 Li, M., Magdassi, S., Gao, Y., and Long, Y. (2017). Hydrothermal synthesis of VO_2 polymorphs: Advantages, challenges and prospects for the application of

energy efficient smart windows. Small 13, 1701147.

28 Wu, C., Feng, F., and Xie, Y. (2013). Design of vanadium oxide structures with controllable electrical properties for energy applications. Chem. Soc. Rev. 42, 5157-5183.

29 Wang, S., Liu, M., Kong, L., Long, Y., Jiang, X., and Yu, A. (2016). Recent progress in VO_2 smart coatings: Strategies to improve the thermochromic properties. Prog. Mater. Sci. 81, 1-54.

30 Wang, S., Owusu, K. A., Mai, L., Ke, Y., Zhou, Y., Hu, P., Magdassi, S., and Long, Y. (2018). Vanadium dioxide for energy conservation and energy storage applications: Synthesis and performance improvement. Appl. Energy 211, 200-217.

31 Granqvist, C. G., and Niklasson, G. A. (2017). Thermochromic oxide-based thin films and nanoparticle composites for energy-efficient glazings. Buildings 7, 3.

32 Guo, F., Chen, S., Chen, Z., Luo, H., Gao, Y., Przybilla, T., Spiecker, E., Osvet, A., Forberich, K., and Brabec, C. J. (2015). Printed smart photovoltaic window integrated with an energy-saving thermochromic layer. Adv. Opt. Mater. 3, 1524-1529.

33 Aschauer, U., Pfenninger, R., Selbach, S. M., Grande, T., and Spaldin, N. A. (2013). Strain-controlled oxygen vacancy formation and ordering in $CaMnO_3$. Phys. Rev. B 88, 054111.

34 Marucco, J. F., Poumellec, B., and Lagnel, F. (1986). Stoichiometry of vanadium dioxide. J Mater. Sci. Lett. 5, 99-100.

35 Chen, C., and Fan, Z. (2009). Changes in VO_2 band structure induced by charge localization and surface segregation. Appl. Phys. Lett. 95, 262106.

36 Cui, Y., Liu, B., Chen, L., Luo, H., and Gao, Y. (2016). Formation energies of intrinsic point defects in monoclinic VO_2 studied by first-principles calculations. AIP Adv. 6, 105301.

37 Chen, L., Cui, Y., Shi, S., Liu, B., Luo, H., and Gao, Y. (2016). First-principles study of the effect of oxygen vacancy and strain on the phase transition temperature of VO_2. RSC Adv. 6, 86872-86879.

38 Chen, L., Wang, X., Wan, D., Cui, Y., Liu, B., Shi, S., Luo, H., and Gao, Y. (2016). Tuning the phase transition temperature, electrical and optical properties of VO_2 by oxygen nonstoichiometry: Insights from first-principles calculations. RSC Adv. 6, 73070-73082.

39 Zhang, S., Kim, I. S., and Lauhon, L. J. (2011). Stoichiometry engineering of monoclinic to rutile phase transition in suspended single crystalline vanadium dioxide nanobeams. Nano Lett. 11, 1443-1447.

40 Zhang, P., Jiang, K., Deng, Q., You, Q., Zhang, J., Wu, J., Hu, Z., and Chu, J. (2015). Manipulations from oxygen partial pressure on the higher energy electronic transition and dielectric function of VO_2 films during a metal-insulator transition process. J. Mater. Chem. C 3, 5033-5040.

41 Jiang, M., Cao, X., Bao, S., Zhou, H., and Jin, P. (2014). Regulation of the phase transition temperature of VO_2 thin films deposited by reactive magnetron sputtering without doping. Thin Solid Films 562, 314-318.

42 Jeong, J., Aetukuri, N., Graf, T., Schladt, T. D., Samant, M. G., and Parkin, S. S. P. (2013). Suppression of metal-insulator transition in VO_2 by electric field-induced oxygen vacancy formation. Science 339, 1402-1405.

43 Chen, S., Wang, X. J., Fan, L., Liao, G., Chen, Y., Chu, W., Song, L., Jiang, J., and Zou, C. (2016). The dynamic phase transition modulation of ion-liquid gating VO_2 thin film: Formation, diffusion, and recovery of oxygen vacancies. Adv. Funct. Mater. 26, 3532-3541.

44 Marezio, M., McWhan, D. B., Remeika, J. P., and Dernier, P. D. (1972). Structural aspects of the metal-insulator transitions in Cr-doped VO_2. Phys. Rev. B 5, 2541-2551.

45 Goodenough, J. B., and Hong, H. Y. P. (1973). Structures and a two-band model for the system $V_{1-x}Cr_xO_2$. Phys. Rev. B 8, 1323-1331.

46 Pouget, J. P., Launois, H., Rice, T. M., Dernier, P., Gossard, A., Villeneuve, G., and Hagenmuller, P. (1974). Dimerization of a linear Heisenberg chain in the insulating phases of $V_{1-x}Cr_xO_2$. Phys. Rev. B 10, 1801-1815.

47 Bruckner, W., Gerlach, U., Bruckner, H. P., Moldenhauer, W., and Oppermann, H. (1976). Influence of nonstoichiometry on the phase transitions in Ga-, Al-, and Fe-doped VO_2. Phys. Stat. Sol. (a) 42, 295-303.

48 Bruckner, W., Bruckner, H. P., Gerlach, U., Thuss, B., and Forsterling, G. (1976). The phase transition M1→T in V1−xGaxO_2. Phys. Stat. Sol. (a) 38, K13-K16.

49 Tang, C., Georgopoulos, P., Fine, M. E., Cohen, J. B., Nygren, M., Knapp, G. S., and Aldred, A. (1985). Local atomic and electronic arrangements in $W_xV_{1-x}O_2$. Phys. Rev. B 31, 1000-1011.

50 Khan, K. A., Niklasson, G. A., and Granqvist, C. G. (1988). Optical properties at

the metal-insulator transition in thermochromic $VO_{2-x}F_x$ thin films. J. Appl. Phys. 64, 3327.

51 Lee, M. H., Kim, M. G., and Song, H. K. (1996). Thermochromism of rapid thermal annealed VO_2 and Sn-doped VO_2 thin films. Thin Solid Films 290-291, 30-33.

52 Burkhardt, W., Christmann, T., Meyer, B. K., Niessner, W., Schalch, D., and Scharmann, A. (1999). W- and F-doped VO_2 films studied by photoelectron spectrometry. Thin Solid Films 345, 229-235.

53 Burkhardt, W., Christmann, T., Franke, S., Kriegseis, W., Meister, D., Meyer, B. K., Niessner, W., Schalch, D., and Scharmann, A. (2002). Tungsten and fluorine co-doping of VO_2 films. Thin Solid Films 402, 226-231.

54 Pan, M., Zhong, H., Wang, S., Li, Z., Chen, X., and Lu, W. (2004). First-principle study on the chromium doping effect on the crystal structure of metallic VO_2. Chem. Phys. Lett. 398, 304-307.

55 Mai, L. Q., Hu, B., Hu, T., Chen, W., and Gu, E. D. (2006). Electrical property of Mo-doped VO_2 nanowire array film by melting-quenching. J. Phys. Chem. B 110, 19083-19086.

56 Piccirillo, C., Binions, R., and Parkin, I. P. (2007). Nb-doped VO_2 thin films prepared by aerosol-assisted chemical vapour deposition. Eur. J. Inorg. Chem. 2007, 4050-4055.

57 Andreev, V. N., Kapralova, V. M., and Klimov, V. A. (2007). Effect of hydrogenation on the metal-semiconductor phase transition in vanadium dioxide thin films. Phys. Solid State 49, 2318-2322.

58 Mlyuka, N. R., Niklasson, G. A., and Granqvist, C. G. (2009). Mg doping of thermochromic VO_2 films enhances the optical transmittance and decreases the metal-insulator transition temperature. Appl. Phys. Lett. 95, 171909.

59 Wu, C., Feng, F., Feng, J., Dai, J., Peng, L., Zhao, J., Yang, J., Si, C., Wu, Z., and Xie, Y. (2011). Hydrogen-incorporation stabilization of metallic VO_2(R) phase to room temperature, displaying promising low-temperature thermoelectric effect. J. Am. Chem. Soc. 133, 13798-13801.

60 Du, J., Gao, Y., Luo, H., Kang, L., Zhang, Z., Chen, Z., and Cao, C. (2011). Significant changes in phase-transition hysteresis for Ti-doped VO_2 films prepared by polymer-assisted deposition. Sol. Energy Mater. Sol. Cells 95, 469-475.

61 Xu, Y., Huang, W., Shi, Q., Zhang, Y., Song, L., and Zhang, Y. (2012). Synthesis and properties of Mo and W ions co-doped porous nano-structured VO_2 films by sol-gel process. J. Sol-Gel Sci. Techn. 64, 493-499.

62 Wei, J., Ji, H., Guo, W., Nevidomskyy, A. H., and Natelson, D. (2012). Hydrogen stabilization of metallic vanadium dioxide in single-crystal nanobeams. Nat. Nanotechnol. 7, 357-362.

63 Tan, X., Yao, T., Long, R., Sun, Z., Feng, Y., Cheng, H., Yuan, X., Zhang, W., Liu, Q., Wu, C., Xie, Y., and Wei, S. (2012). Unraveling metal-insulator transition mechanism of VO_2 triggered by tungsten doping. Sci. Rep. 2, 466.

64 Hu, S., Li, S. Y., Ahuja, R., Granqvist, C. G., Hermansson, K., Niklasson, G. A., and Scheicher, R. H. (2012). Optical properties of Mg-doped VO_2: Absorption measurements and hybrid functional calculations. Appl. Physi. Lett. 101, 201902.

65 Gao, Y., Cao, C., Dai, L., Luo, H., Kanehira, M., Ding, Y., and Wang, Z. L. (2012). Phase and shape controlled VO_2 nanostructures by antimony doping. Energy Environ. Sci. 5, 8708-8715.

66 Zhou, J., Gao, Y., Liu, X., Chen, Z., Dai, L., Cao, C., Luo, H., Kanahira, M., Sun, C., and Yan, L. (2013). Mg-doped VO_2 nanoparticles: Hydrothermal synthesis, enhanced visible transmittance and decreased metal-insulator transition temperature. Phys. Chem. Chem. Phys. 15, 7505-7511.

67 Zhang, Y., Zhang, J., Zhang, X., Huang, C., Zhong, Y., and Deng, Y. (2013). The additives W, Mo, Sn and Fe for promoting the formation of VO_2(M) and its optical switching properties. Mater. Lett. 92, 61-64.

68 Zhang, J., He, H., Xie, Y., and Pan, B. (2013). Giant reduction of the phase transition temperature for beryllium doped VO_2. Phys. Chem. Chem. Phys. 15, 4687-4690.

69 Song, L., Zhang, Y., Huang, W., Shi, Q., Li, D., Zhang, Y., and Xu, Y. (2013). Preparation and thermochromic properties of Ce-doped VO_2 films. Mater. Res. Bull. 48, 2268-2271.

70 Li, S. Y., Mlyuka, N. R., Primetzhofer, D., Hallén, A., Possnert, G., Niklasson, G. A., and Granqvist, C. G. (2013). Bandgap widening in thermochromic Mg-doped VO_2 thin films: Quantitative data based on optical absorption. Appl. Phys. Lett. 103, 161907.

71 Dai, L., Chen, S., Liu, J., Gao, Y., Zhou, J., Chen, Z., Cao, C., Luo, H., and Kanehira, M. (2013). F-doped VO_2 nanoparticles for thermochromic

energy-saving foils with modified color and enhanced solar-heat shielding ability. Phys. Chem. Chem. Phys. 15, 11723-11729.

72 Chen, S., Dai, L., Liu, J., Gao, Y., Liu, X., Chen, Z., Zhou, J., Cao, C., Han, P., Luo, H., and Kanahira, M. (2013). The visible transmittance and solar modulation ability of VO_2 flexible foils simultaneously improved by Ti doping: An optimization and first principle study. Phys. Chem. Chem. Phys. 15, 17537-17543.

73 Zhao, Y., Karaoglan, B. G., Pan, X., Holtz, M., Bernussi, A. A., and Fan, Z. (2014). Hydrogen-doping stabilized metallic VO_2(R) thin films and their application to suppress Fabry-Perot resonances in the terahertz regime. Appl. Phys. Lett. 104, 241901.

74 Zhang, W., Wang, K., Fan, L., Liu, L., Guo, P., Zou, C., Wang, J., Qian, H., Ibrahim, K., Yan, W., Xu, F., and Wu, Z. (2014). Hole carriers doping effect on the metal-insulator transition of N-incorporated vanadium dioxide thin films. J. Phys. Chem. C 118, 12837-12844.

75 Zhang, J. J., He, H. Y., Xie, Y., and Pan, B. C. (2014). Boron-tuning transition temperature of vanadium dioxide from rutile to monoclinic phase. J. Chem. Phys. 141, 194707.

76 Wu, Y., Fan, L., Chen, S., Chen, S., Chen, F., Zou, C., and Wu, Z. (2014). A novel route to realize controllable phases in an aluminum (Al^{3+})-doped VO_2 system and the metal-insulator transition modulation. Mater. Lett. 127, 44-47.

77 Warnick, K. H., Wang, B., and Pantelides, S. T. (2014). Hydrogen dynamics and metallic phase stabilization in VO_2. Appl. Phys. Lett. 104, 101913.

78 Sun, C., Yan, L., Yue, B., Liu, H., and Gao, Y. (2014). The modulation of metal-insulator transition temperature of vanadium dioxide: A density functional theory study. J. Mater. Chem. C 2, 9283-9293.

79 Ren, Q., Wan, J., and Gao, Y. (2014). Theoretical study of electronic properties of X-doped (X = F, Cl, Br, I) VO_2 nanoparticles for thermochromic energy-saving foils. J. Phys. Chem. A 118, 11114-11118.

80 Miyazaki, K., Shibuya, K., Suzuki, M., Wado, H., and Sawa, A. (2014). Correlation between thermal hysteresis width and broadening of metal-insulator transition in Cr- and Nb-doped VO_2 films. Jpn. J. Appl. Phys. 53, 71102.

81 Li, S. Y., Niklasson, G. A., and Granqvist, C. G. (2014). Thermochromic undoped and Mg-doped VO_2 thin films and nanoparticles: Optical properties and

performance limits for energy efficient windows. J. Appl. Phys. 115, 053513.

82 Hur, M. G., Masaki, T., and Yoon, D. H. (2014). Thermochromic properties of Sn, W Co-doped VO_2 nanostructured thin film deposited by pulsed laser deposition. J. Nanosci. Nanotechno. 14, 8941-8945.

83 Cao, X., Wang, N., Magdassi, S., Mandler, D., and Long, Y. (2014). Europium doped vanadium dioxide material: Reduced phase transition temperature, enhanced luminous transmittance and solar modulation. Sci. Adv. Mater. 6, 558-561.

84 Zhang, H., Wu, Z., Niu, R., Wu, X. F., He, Q., and Jiang, Y. D. (2015). Metal-insulator transition properties of sputtered silicon-doped and un-doped vanadium dioxide films at terahertz range. Appl. Surf. Sci. 331, 92-97.

85 Wu, Y., Fan, L., Liu, Q., Chen, S., Huang, W., Chen, F., Liao, G., Zou, C., and Wu, Z. (2015). Decoupling the lattice distortion and charge doping effects on the phase transition behavior of VO_2 by Titanium (Ti^{4+}) doping. Sci Rep. 5, 9328.

86 Wang, N., Liu, S., Zeng, X. T., Magdassi, S., and Long, Y. (2015). Mg/W-codoped vanadium dioxide thin films with enhanced visible transmittance and low phase transition temperature. J. Mater. Chem. C 3, 6771-6777.

87 Miller, M. J., and Wang, J. (2015). Influence of Na diffusion on thermochromism of vanadium oxide films and suppression through mixed-alkali effect. Mater. Sci. Eng. B 200, 50-58.

88 Li, W., Ji, S., Qian, K., and Jin, P. (2015). Preparation and characterization of VO_2(M)-SnO_2 thermochromic films for application as energy-saving smart coatings. J. Colloid. Interface Sci. 456, 166-173.

89 He, X., Zeng, Y., Xu, X., Gu, C., Chen, F., Wu, B., Wang, C., Xing, H., Chen, X., and Chu, J. (2015). Orbital change manipulation metal-insulator transition temperature in W-doped VO_2. Phys. Chem. Chem. Phys. 17, 11638-11646.

90 Gu, D., Sun, Z., Zhou, X., Guo, R., Wang, T., and Jiang, Y. D. (2015). Effect of yttrium-doping on the microstructures and semiconductor-metal phase transition characteristics of polycrystalline VO_2 thin films. Appl. Surf. Sci. 359, 819-825.

91 Dietrich, M. K., Kramm, B. G., Becker, M., Meyer, B. K., Polity, A., and Klar, P. J. (2015). Influence of doping with alkaline earth metals on the optical properties of thermochromic VO_2. J. Appl. Phys. 117, 185301.

92 Cui, Y., Shi, S., Chen, L., Luo, H., and Gao, Y. (2015). Hydrogen-doping induced reduction in the phase transition temperature of VO_2: A first-principles

study. Phys. Chem. Chem. Phys. 17, 20998-21004.

93 Wu, X., Wu, Z., Ji, C., Zhang, H., Su, Y., Huang, Z., Gou, J., Wei, X., Wang, J., and Jiang, Y. (2016). THz transmittance and electrical properties tuning across IMT in vanadium dioxide films by Al doping. ACS Appl. Mater. Interfaces 8, 11842-11850.

94 Wu, X. F., Wu, Z. M., Liu, Z. J., Ji, C. H., Huang, Z. H., Su, Y. J., Gou, J., Wang, J., and Jiang, Y. D. (2016). Rebound effect of IMT properties by different doping form in Si-doped vanadium dioxide films. Appl. Phys. Lett. 109, 111903.

95 Wilkinson, M., Kafizas, A., Bawaked, S. M., Obaid, A. Y., Al-Thabaiti, S. A., Basahel, S. N., Carmalt, C. J., and Parkin, I. P. (2013). Combinatorial atmospheric pressure chemical vapor deposition of graded TiO_2-VO_2 mixed-phase composites and their dual functional property as self-cleaning and photochromic window coatings. ACS Comb. Sci. 15, 309-319.

96 Yuan, X., Zhang, Y., Abtew, T. A., Zhang, P., and Zhang, W. (2012). VO_2: Orbital competition, magnetism, and phase stability. Phys. Rev. B 86, 235103.

97 Cyrot, M. (1972). Theory of Mott transition: Applications to transition metal oxides. Journal de Physique 33, 125-134.

98 Cui, Y., Wang, Y., Liu, B., Luo, H., and Gao, Y. (2016). First-principles study on the phase transition temperature of X-doped (X = Li, Na or K) VO_2. RSC Adv. 6, 64394-64399.

99 Zhang, J., He, H., Xie, Y., and Pan, B. (2013). Theoretical study on the tungsten-induced reduction of transition temperature and the degradation of optical properties for VO_2. J. Chem. Phys. 138, 114705.

100 Hu, L. T., Tao, H. Z., Chen, G. H., Pan, R. K., Wan, M. N., Xiong, D. H., and Zhao, X. J. (2016). Porous W-doped VO_2 films with simultaneously enhanced visible transparency and thermochromic properties. J. Sol-Gel Sci. Techn. 77, 85-93.

101 Li, D., Li, M., Pan, J., Luo, Y., Wu, H., Zhang, Y., and Li, G. (2014). Hydrothermal synthesis of Mo-doped VO_2/TiO_2 composite nanocrystals with enhanced thermochromic performance. ACS Appl. Mater. Interfaces 6, 6555-6561.

102 Liu, D., Cheng, H., Xing, X., Zhang, C., and Zheng, W. (2016). Thermochromic properties of W-doped VO_2 thin films deposited by aqueous sol-gel method for adaptive infrared stealth application. Infrared Phys. Technol. 77, 339-343.

103 Shen, N., Chen, S., Chen, Z., Liu, X., Cao, C., Dong, B., Luo, H., Liu, J., and Gao, Y. (2014). The synthesis and performance of Zr-doped and W-Zr-codoped VO_2 nanoparticles and derived flexible foils. J. Mater. Chem. A 2, 15087-15093.

104 Wang, N., Duchamp, M., Dunin-Borkowsk, R. E., Liu, S., Zeng, X., Cao, X., and Long, Y. (2016). Terbium-doped VO_2 thin films: Reduced phase transition temperature and largely enhanced luminous transmittance. Langmuir 32, 759-764.

105 Wang, N., Shun, N. T. C., Duchamp, M., Dunin-Borkowski, R. E., Li, Z., and Long, Y. (2016). Effect of lanthanum doping on modulating the thermochromic properties of VO_2 thin films. RSC Adv. 6, 48455-48461.

106 Cui, Y., Cao, C., Chen, Z., Luo, H., and Gao, Y. (2017). Atomic and electronic structures of thermochromic VO_2 with Sb-doping. Comp. Mater. Sci. 130, 103-108.

107 Ladd, L. A., and Paul, W. (1969). Optical and transport properties of high quality crystals of V_2O_4 near the metallic transition temperature. Solid State Commun. 7, 425-428.

108 Arcangeletti, E., Baldassarre, L., Di Castro, D., Lupi, S., Malavasi, L., Marini, C., Perucchi, A., and Postorino, P. (2007). Evidence of a pressure-induced metallization process in monoclinic VO_2. Phys. Rev. Lett. 98, 196406.

109 Marini, C., Arcangeletti, E., Di Castro, D., Baldassarre, L., Perucchi, A., Lupi, S., Malavasi, L., Boeri, L., Pomjakushina, E., Conder, K., and Postorino, P. (2008). Optical properties of $V_{1-x}Cr_xO_2$ compounds under high pressure. Phys. Rev. B 77, 235111.

110 Marini, C., Bendele, M., Joseph, B., Kantor, I., Mitrano, M., Mathon, O., Baldini, M., Malavasi, L., Pascarelli, S., and Postorino, P. (2014). Probing the electronic and local structural changes across the pressure-induced insulator-to-metal transition in VO_2. EPL 108, 36003.

111 Okuyama, D., Nakano, M., Takeshita, S., Ohsumi, H., Tardif, S., Shibuya, K., Hatano, T., Yumoto, H., Koyama, T., Ohashi, H., Takata, M., Kawasaki, M., Arima, T., Tokura, Y., and Iwasa, Y. (2014). Gate-tunable gigantic lattice deformation in VO_2. Appl. Phys. Lett. 104, 023507.

112 Cao, J., Ertekin, E., Srinivasan, V., Fan, W., Huang, S., Zheng, H., Yim, J. W. L., Khanal, D. R., Ogletree, D. F., Grossmanan, J. C., and Wu, J. (2009). Strain engineering and one-dimensional organization of metal-insulator domains in

single-crystal vanadium dioxide beams. Nat. Nanotechnol. 4, 732-737.

113 Case, F. C. (1988). The influence of substrate temperature on the optical properties of ion-assisted reactively evaporated vanadium oxide thin films. J. Vac. Sci. Technol. A. 6, 2010-2014.

114 Jin, P., Yoshimura, K., and Tanemura, S. (1997). Dependence of microstructure and thermochromism on substrate temperature for sputter-deposited VO_2 epitaxial films. J. Vac. Sci. Technol. A 15, 1113-1117.

115 Muraoka, Y., and Hiroi, Z. (2002). Metal-insulator transition of VO_2 thin films grown on TiO_2 (001) and (110) substrates. Appl. Phys. Lett. 80, 583-585.

116 Muraoka, Y., Ueda, Y., and Hiroi, Z. (2002). Large modification of the metal-insulator transition temperature in strained VO_2 films grown on TiO_2 substrates. J. Phys. Chem. Solids 63, 965-967.

117 Wu, J., Gu, Q., Guiton, B. S., de Leon, N. P., Lian, O., and Park, H. (2006). Strain-induced self organization of metal-insulator domains in single-crystalline VO_2 nanobeams. Nano Lett. 6, 2313-2317.

118 Chang, S., Park, J. B., Lee, G., Kim, H. J., Lee, J., Bae, T., Han, Y., Park, T. J., Huh, Y. S., and Hong, W. (2014). In situ probing of doping- and stress-mediated phase transitions in a single-crystalline VO_2 nanobeam by spatially resolved Raman spectroscopy. Nanoscale 6, 8068-8074.

119 Kim, M. H., Lee, B., Lee, S., Larson, C., Baik, J. M., Yavuz, C. T., Seifert, S., Vajda, S., Winans, R. E., Moskovits, M., Stucky, G. D., and Wodtke, A. M. (2009). Growth of metal oxide nanowires from supercooled liquid nanodroplets. Nano Lett. 9, 4138-4146.

120 Rama, N., and Ramachandra Rao, M. S. (2010). Synthesis and study of electrical and magnetic properties of vanadium oxide micro and nanosized rods grown using pulsed laser deposition technique. Solid State Commun. 150, 1041-1044.

121 Nag, J., and Jr. Haglund, R. F. (2008). Synthesis of vanadium dioxide thin films and nanoparticles. J. Phys.Condens. Matter 20, 264016.

122 Zheng, C. M., Zhang, J. L., Luo, G. B., Ye, J. Q., and Wu, M. M. (2000). Preparation of vanadium dioxide powders by thermolysis of a precursor at low temperature. J. Mater. Sci. 35, 3425-3429.

123 Peng, Z., Jiang, W., and Liu, H. (2007). Synthesis and electrical properties of tungsten-doped vanadium dioxide nanopowders by thermolysis. J. Phys. Chem. C 111, 1119-1122.

124 Qi, J., Ning, G., and Lin, Y. (2008). Synthesis, characterization, and thermodynamic parameters of vanadium dioxide. Mater. Res. Bull. 43, 2300-2307.

125 Cao, C., Gao, Y., and Luo, H. (2008). Pure single-crystal rutile vanadium dioxide powders: Synthesis, mechanism and phase-transformation property. J. Phys. Chem. C 112, 18810-18814.

126 Ji, S., Zhao, Y., Zhang, F., and Jin, P. (2010). Direct formation of single crystal VO_2(R) nanorods by one-step hydrothermal treatment. J. Cryst. Growth 312, 282-286.

127 Dai, L., Cao, C., Gao, Y., and Luo, H. (2011). Synthesis and phase transition behavior of undoped VO_2 with a strong nano-size effect. Sol. Energy Mater. Sol. Cells 95, 712-715.

128 Whittaker, L., Velazquez, J. M., and Banerjee, S. (2011). A VO-seeded approach for the growth of star-shaped VO_2 and V_2O_5 nanocrystals: Facile synthesis, structural characterization, and elucidation of electronic structure. Crystengcomm. 13, 5328-5336.

129 Zhou, Y., Ji, S., Li, Y., Gao, Y., Luo, H., and Jin, P. (2014). Microemulsion-based synthesis of $V_{1-x}W_xO_2$@SiO_2 core-shell structures for smart window applications. J. Mater. Chem. C 2, 3812-3819.

130 Wu, C., Feng, F., Feng, J., Dai, J., Yang, J., and Xie, Y. (2011). Ultrafast solid-state transformation pathway from new-phased goethite VOOH to paramontroseite VO_2 to rutile VO_2(R). J. Phys. Chem. C 115, 791-799.

131 Wu, C., Dai, J., Zhang, X., Yang, J., Qi, F., Gao, C., and Xie, Y. (2010). Direct confined-space combustion forming monoclinic vanadium dioxides. Angew. Chem. Int. Edit. 49, 134-137.

132 Xu, C. L., Ma, X., Liu, X., Qiu, W. Y., and Su, Z. X. (2004). A novel reduction-hydrolysis method of preparing VO_2 nanopowders. Mater. Res. Bull. 39, 881-886.

133 Kam, K. C., and Cheetham, A. K. (2006). Thermochromic VO_2 nanorods and other vanadium oxides nanostructures. Mater. Res. Bull. 41, 1015-1021.

134 Zhang, K., Liu, X., Su, Z., and Li, H. (2007). VO_2(R) nanobelts resulting from the irreversible transformation of VO_2(B) nanobelts. Mater. Lett. 61, 2644-2647.

135 Yamamoto, S., Kasai, N., and Shimakawa, Y. (2009). Preparation of monodisperse and spherical rutile VO_2 fine particles. Chem. Mater. 21, 198-200.

136 Whittaker, L., Zhang, H., and Banerjee, S. (2009). VO_2 nanosheets exhibiting a well-defined metal-insulator phase transition. J. Mater. Chem. 19, 2968-2974.

137 Zhang, Y., Fan, M., Niu, F., Wu, W., Huang, C., Liu, X., Li, H., and Liu, X. (2012). Belt-like VO_2(M) with a rectangular cross section: A new route to prepare, the phase transition and the optical switching properties. Curr. Appl. Phys. 12, 875-879.

138 Liu, L., Cao, F., Yao, T., Xu, Y., Zhou, M., Qu, B., Pan, B., Wu, C., Wei, S., and Xie, Y. (2012). New-phase VO_2 micro/nanostructures: Investigation of phase transformation and magnetic property. New J. Chem. 36, 619-625.

139 Zhang, S., Fu, J., Su, Q., Fu, C., and Li, X. (2015). Preparation of VO_2 superfine powders by a redox method and in situ characterization on the reversible phase transition. Rare Metal Mat. Eng. 44, 738-742.

140 Liu, X., Huang, C., Yi, S., Xie, G., Li, H., and Luo, Y. (2007). A new solvothermal method of preparing VO_2 nanosheets and petaloid clusters. Solid State Commun. 144, 259-263.

141 Ye, J., Zhou, L., Liu, F., Qi, J., Gong, W., Lin, Y., and Ning, G. (2010). Preparation, characterization and properties of thermochromic tungsten-doped vanadium dioxide by thermal reduction and annealing. J. Alloy. Compd. 504, 503-507.

142 Gui, Z., Fan, R., Mo, W. Q., Chen, X. H., Yang, L., Zhang, S. Y., Hu, Y., Wang, Z. Z., and Fan, W. C. (2002). Precursor morphology controlled formation of rutile VO_2 nanorods and their self-assembled structure. Chem. Mater. 14, 5053-5056.

143 Chen, J., Liu, X., Dai, L., Chen, L., Gao, Y., and Chen, N. (2012). Deoxidization of V_2O_5 powder into VO_2 assisted by an electrochemical lithium intercalation technique. Int. J. Appl. Ceram. Technol. 9, 942-946.

144 Gao, Y., Cao, C., Dai, L., Luo, H., Kanehira, M., Ding, Y., and Wang, Z. (2012). Phase and shape controlled VO_2 nanostructures by antimony doping. Energy Environ. Sci. 5, 8708-8715.

145 Ji, H., Liu, D., Cheng, H., Zhang, C., and Yang, L. (2018). Vanadium dioxide nanopowders with tunable emissivity for adaptive infrared camouflage in both thermal atmospheric windows. Sol. Energy Mater. Sol. Cells 175, 96-101.

146 Granqvist, C. G. (2007). Transparent conductors as solar energy materials: A panoramic review. Sol. Energy Mater. Sol. Cells 91, 1529-1598.

147 Li, S. Y., Niklasson, G. A., and Granqvist, C. G. (2010). Nanothermochromics: Calculations for VO_2 nanoparticles in dielectric hosts show much improved luminous transmittance and solar energy transmittance modulation. J. Appl. Phys. 108, 63525.

148 Li, S. Y., Niklasson, G. A., and Granqvist, C. G. (2011). Nanothermochromics with VO_2-based core-shell structures: Calculated luminous and solar optical properties. J. Appl. Phys. 109, 113515.

149 Laaksonen, K., Li, S. Y., Puisto, S. R., Rostedt, N. K. J., Ala-Nissila, T., Granqvist, C. G., Nieminen, R. M., and Niklasson, G. A. (2014). Nanoparticles of TiO_2 and VO_2 in dielectric media: Conditions for low optical scattering, and comparison between effective medium and four-flux theories. Sol. Energy Mater. Sol. Cells 130, 132-137.

150 Chen, Z., Gao, Y., Kang, L., Cao, C., Chen, S., and Luo, H. (2014). Fine crystalline VO_2 nanoparticles: Synthesis, abnormal phase transition temperatures and excellent optical properties of a derived VO_2 nanocomposite foil. J. Mater. Chem. A 2, 2718-2727.

151 Shen, N., Dong, B., Cao, C., Chen, Z., Luo, H., and Gao, Y. (2015). Solid-state-reaction synthesis of VO_2 nanoparticles with low phase transition temperature, enhanced chemical stability and excellent thermochromic properties. RSC Adv. 5, 108015-108022.

152 Gao, Y., Wang, S., Kang, L., Chen, Z., Du, J., Liu, X., Luo, H., and Kanehira, M. (2012). VO_2-Sb:SnO_2 composite thermochromic smart glass foil. Energy Environ. Sci. 5, 8234-8237.

153 Gao, Y., Wang, S., Luo, H., Dai, L., Cao, C., Liu, Y., Chen, Z., and Kanehira, M. (2012). Enhanced chemical stability of VO_2 nanoparticles by the formation of SiO_2/VO_2 core/shell structures and the application to transparent and flexible VO_2-based composite foils with excellent thermochromic properties for solar heat control. Energy Environ. Sci. 5, 6104-6110.

154 Zhou, Y., Huang, A., Li, Y., Ji, S., Gao, Y., and Jin, P. (2013). Surface plasmon resonance induced excellent solar control for VO_2@SiO_2 nanorods-based thermochromic foils. Nanoscale 5, 9208-9213.

155 Zhu, J., Zhou, Y., Wang, B., Zheng, J., Ji, S., Yao, H., Luo, H., and Jin, P. (2015). Vanadium dioxide nanoparticle-based thermochromic smart coating: High luminous transmittance, excellent solar regulation efficiency, and near room

temperature phase transition. ACS Appl. Mater. Interfaces 7, 27796-27803.

156 Ji, H., Liu, D., Zhang, C., and Cheng, H. (2018). VO_2/ZnS core-shell nanoparticle for the adaptive infrared camouflage application with modified color and enhanced oxidation resistance. Sol. Energy Mater. Sol. Cells 176, 1-8.

157 Liu, C., Cao, X., Kamyshny, A., Law, J. Y., Magdassi, S., and Long, Y. (2014). VO_2/Si-Al gel nanocomposite thermochromic smart foils: Largely enhanced luminous transmittance and solar modulation. J. Colloid Interface Sci. 427, 49-53.

158 Lu, Q., Liu, C., Wang, N., Magdassi, S., Mandler, D., and Long, Y. (2016). Periodic micro-patterned VO_2 thermochromic films by mesh printing. J. Mater. Chem. C 4, 8385-8391.

159 Moot, T., Palin, C., Mitran, S., Cahoon, J. F., and Lopez, R. (2016). Designing plasmon-enhanced thermochromic films using a vanadium dioxide nanoparticle elastomeric composite. Adv. Opt. Mater. 4, 578-583.

160 Chen, Z., Cao, C., Chen, S., Luo, H., and Gao, Y. (2014). Crystallised mesoporous TiO_2(A)-VO_2(M/R) nanocomposite films with self-cleaning and excellent thermochromic properties. J. Mater. Chem. A 2, 11874-11884.

161 Zhou, Y., Cai, Y. F., Hu, X., and Long, Y. (2014). Temperature-responsive hydrogel with ultra-large solar modulation and high luminous transmission for “smart window” applications. J. Mater. Chem. A 2, 13550-13555.

162 Zhou, Y., Cai, Y. F., Hu, X., and Long, Y. (2015). VO_2/hydrogel hybrid nanothermochromic material with ultra-high solar modulation and luminous transmission. J. Mater. Chem. A 3, 1121-1126.

163 Yang, Y. S., Zhou, Y., Chiang, F., and Long, Y. (2017). Tungsten doped VO_2/microgels hybrid thermochromic material and its smart window application. RSC Adv. 7, 7758-7762.

164 Zhu, J. T., Huang, A. B., Ma, H. B., Ma, Y. N., Tong, K., Ji, S. D., Bao, S. H., Cao, X., and Jin, P. (2016). Composite film of vanadium dioxide nanoparticles and ionic liquid-nickel-chlorine complexes with excellent visible thermochromic performance. ACS Appl. Mater. Interfaces 8, 29742-29748.

165 Zhu, J. T., Huang, A. B., Ma, H. B., Bao, S. H., Ji, S. D., and Jin, P. (2016). Solar-thermochromism of a hybrid film of VO_2 nanoparticles and Co^{II}-Br-TMP complexes. RSC Adv. 6, 67396-67399.

166 Zhu, J. T., Huang, A. B., Ma, H. B., Chen, Y. X., Zhang, S. P., Ji, S. D., Bao, S.

H., and Jin, P. (2017). Hybrid films of VO_2 nanoparticles and a nickel(II)-based ligand exchange thermochromic system: Excellent optical performance with a temperature responsive colour change. New J. Chem. 41, 830-835.

167 Hild, E., and Grofcsik, A. (1978). Calculation of IR reflection spectra of inhomogeneously doped semiconductors. Infrared Phys. 18, 23-33.

168 Hild, E., and Evans, M. W. (1986). Calculation of the infrared reflection spectra of inhomogeneously doped silicon semiconductor layers at an arbitrary angle of incidence. J. Appl. Phys. 59, 1822-1828.

169 Deak, A., Hild, E., Kovacs, A. L., and Horvolgyi, Z. (2007). Contact angle determination of nanoparticles: Film balance and scanning angle reflectometry studies. Phys. Chem. Chem. Phys. 9, 6359-6370.

170 Hild, E., and Deák, A. (2007). Use of the optical admittance function and its WKB approximation to simulate and evaluate transmittance spectra of graded-index colloidal films. J. Opt. A-Pure Appl. Opt. 9, 920.

171 Kang, L., Gao, Y., Luo, H., Chen, Z., Du, J., and Zhang, Z. (2011). Nanoporous thermochromic VO_2 films with low optical constants, enhanced luminous transmittance and thermochromic properties. ACS Appl. Mater. Interfaces 3, 135-138.

172 Ding, S., Liu, Z., Li, D., Zhao, W., Wang, Y., Wan, D., and Huang, F. (2013). Tunable assembly of vanadium dioxide nanoparticles to create porous film for energy-saving applications. ACS Appl. Mater. Interfaces 5, 1630-1635.

173 Xu, Y. J., Huang, W. X., Shi, Q. W., Zhang, Y. B., Wu, J., and Song, L. W. (2013). Shape-dependent thermochromic phenomenon in porous nanostructured VO_2 films. Mater. Res. Bull. 48, 4146-4149.

174 Xu, Y. J., Huang, W. X., Shi, Q. W., Zhang, Y. B., Wu, J., and Song, L. W. (2013). Porous nano-structured VO_2 films with different surfactants: Synthesis mechanisms, characterization, and applications. J. Mater. Sci.-Mater. Electron. 24, 3823-3829.

175 Cao, X., Wang, N., Law, J. Y., Loo, S., Magdassi, S., and Long, Y. (2014). Nanoporous thermochromic VO_2(M) thin films: Controlled porosity, largely enhanced luminous transmittance and solar modulating ability. Langmuir 30, 1710-1715.

176 Wang, N., Huang, Y. Z., Magdassi, S., Mandler, D., Liu, H., and Long, Y. (2013). Formation of VO_2 zero-dimensional/nanoporous layers with large supercooling

effects and enhanced thermochromic properties. RSC Adv. 3, 7124-7128.

177 Liu, M., Su, B., Kaneti, Y., Chen, Z., Tang, Y., Yuan, Y., Gao, Y., Jiang, L., Jiang, X., and Yu, A. (2017). Dual-phase transformation: Spontaneous self-template surface-patterning strategy for ultra-transparent VO_2 solar modulating coatings. ACS Nano 11, 407-415.

178 Zhang, J., Jin, H., Chen, Z., Cao, M., Chen, P., Dou, Y., Zhao, Y., and Li, J. (2015). Self-assembling VO_2 nanonet with high switching performance at wafer-scale. Chem. Mater. 27, 7419-7424.

179 Liu, C., Balin, I., Magdassi, S., Abdulhalim, I., and Long, Y. (2015). Vanadium dioxide nanogrid films for high transparency smart architectural window applications. Opt. Express 23, A124-A132.

180 Liu, C., Long, Y., Magdassi, S., and Mandler, D. (2017). Ionic strength induced electrodeposition: A universal approach for nanomaterial deposition at selective areas. Nanoscale 9, 485-490.

181 Ye, X., and Qi, L. (2011). Two-dimensionally patterned nanostructures based on monolayer colloidal crystals: Controllable fabrication, assembly, and applications. Nano Today 6, 608-631.

182 Zhou, M., Bao, J., Tao, M., Zhu, R., Lin, Y., Zhang, X., and Xie, Y. (2013). Periodic porous thermochromic VO_2(M) films with enhanced visible transmittance. Chem. Commun. 49, 6021-6023.

183 Ke, Y., Wen, X., Zhao, D., Che, R., Xiong, Q., and Long, Y. (2017). Controllable fabrication of two-dimensional patterned VO_2 nanoparticle, nanodome, and nanonet arrays with tunable temperature-dependent localized surface plasmon resonance. ACS Nano 11, 7542-7551.

184 Yu, K., Fan, T., Lou, S., and Zhang, D. (2013). Biomimetic optical materials: Integration of nature's design for manipulation of light. Prog. Mater. Sci. 58, 825-873.

185 Li, Y. F., Zhang, J. H., Zhu, S. J., Dong, H. P., Jia, F., Wang, Z. H., Sun, Z. Q., Zhang, L., Li, Y., Li, H. B., Xu, W. Q., and Yang, B. (2009). Biomimetic surfaces for high-performance optics. Adv. Mater. 21, 4731-4734.

186 Vukusic, P., and Sambles, J. R. (2003). Photonic structures in biology. Nature 424, 852-855.

187 Taylor, A., Parkin, I., Noor, N., Tummeltshammer, C., Brown, M. S., and Papakonstantinou, I. (2013). A bioinspired solution for spectrally selective

thermochromic VO_2 coated intelligent glazing. Opt. Express 21, A750-A764.

188 Qian, X., Wang, N., Li, Y., Zhang, J., Xu, Z., and Long, Y. (2014). Bioinspired multifunctional vanadium dioxide: Improved thermochromism and hydrophobicity. Langmuir 30, 10766-10771.

189 Yablonovitch, E. (1987). Inhibited spontaneous emission in solid-state physics and electronics. Phys. Rev. Lett. 58, 2059-2062.

190 Aguirre, C. I., Reguera, E., and Stein, A. (2010). Tunable colors in opals and inverse opal photonic crystals. Adv. Funct. Mater. 20, 2565-2578.

191 Ke, Y., Balin, I., Wang, N., Lu, Q., Tok, A. T. Y., White, T. J., Magdassi, S., Abdulhalim, I., and Long, Y. (2016). Two-dimensional SiO_2/VO_2 photonic crystals with statically visible and dynamically infrared modulated for smart window deployment. ACS Appl. Mater. Interfaces 8, 33112-33120.

192 Saitzek, S., Guinneton, F., Sauques, L., Aguir, K., and Gavarri, J. (2007). Thermochromic CeO_2-VO_2 bilayers: Role of ceria coating in optical switching properties. Opt. Mater. 30, 407-415.

193 Liu, C., Wang, N., and Long, Y. (2013). Multifunctional overcoats on vanadium dioxide thermochromic thin films with enhanced luminous transmission and solar modulation, hydrophobicity and anti-oxidation. Appl. Surf. Sci. 283, 222-226.

194 Evans, P., Pemble, M. E., Sheel, D. W., and Yates, H. M. (2007). Multi-functional self-cleaning thermochromic films by atmospheric pressure chemical vapour deposition. J. Photochem. Photobiol. A-Chem. 189, 387-397.

195 Raut, H. K., Ganesh, V. A., Nair, A. S., and Ramakrishna, S. (2011). Anti-reflective coatings: A critical, in-depth review. Energy Environ. Sci. 4, 3779-3804.

196 Tazawa, M., Jin, P., and Tanemura, S. (1998). Optical constants of V1-xWxO_2 films. Appl. Optics 37, 1858-1861.

197 Xu, G., Jin, P., Tazawa, M., and Yoshimura, K. (2004). Optimization of antireflection coating for VO_2-based energy efficient window. Sol. Energy Mater. Sol. Cells 83, 29-37.

198 Jin, P., Xu, G., Tazawa, M., and Yoshimura, K. (2002). A VO_2-based multifunctional window with highly improved luminous transmittance. Jpn. J. Appl. Phys. 41, L278-L280.

199 Koo, H., Shin, D., Bae, S., Ko, K., Chang, S., and Park, C. (2014). The effect of CeO_2 antireflection layer on the optical properties of thermochromic VO_2 film

for smart window system. J. Mater. Eng. Perform. 23, 402-407.

200 Zhang, Z., Gao, Y., Luo, H., Kang, L., Chen, Z., Du, J., Kanehira, M., Zhang, Y., and Wang, Z. L. (2011). Solution-based fabrication of vanadium dioxide on F:SnO_2 substrates with largely enhanced thermochromism and low-emissivity for energy-saving applications. Energy Environ. Sci. 4, 4290-4297.

201 Jin, P., Xu, G., Tazawa, M., and Yoshimura, K. (2003). Design, formation and characterization of a novel multifunctional window with VO_2 and TiO_2 coatings. Appl. Phys. A-Mater. Sci. Process 77, 455-459.

202 Liu, C., Wang, S., Zhou, Y., Yang, H., Lu, Q., Mandler, D., Magdassi, S., Tay, C. Y., and Long, Y. (2018). Index-tunable anti-reflection coatings: Maximizing solar modulation ability for vanadium dioxide-based smart thermochromic glazing. J. Alloy. Compd. 731, 1197-1207.

203 Chen, Z., Gao, Y., Kang, L., Du, J., Zhang, Z., Luo, H., Miao, H., and Tan, G. (2011). VO_2-based double-layered films for smart windows: Optical design, all-solution preparation and improved properties. Sol. Energy Mater. Sol. Cells 95, 2677-2684.

204 Mlyuka, N. R., Niklasson, G. A., and Granqvist, C. G. (2009). Thermochromic multilayer films of VO_2 and TiO_2 with enhanced transmittance. Sol. Energy Mater. Sol. Cells 93, 1685-1687.

205 Kang, L., Gao, Y., Luo, H., Wang, J., Zhu, B., Zhang, Z., Du, J., Kanehira, M., and Zhang, Y. (2011). Thermochromic properties and low emissivity of ZnO:Al/VO_2 double-layered films with a lowered phase transition temperature. Sol. Energy Mater. Sol. Cells 95, 3189-3194.

206 Zhang, Z., Gao, Y., Kang, L., Du, J., and Luo, H. (2010). Effects of a TiO_2 buffer layer on solution-deposited VO_2 films: Enhanced oxidization durability. J. Phys. Chem. C 114, 22214-22220.

207 Zheng, J., Bao, S., and Jin, P. (2015). TiO_2(R)/VO_2(M)/TiO_2(A) multilayer film as smart window: Combination of energy-saving, antifogging and self-cleaning functions. Nano Energy 11, 136-145.

208 Zhang, Z., Gao, Y., Chen, Z., Du, J., Cao, C., Kang, L., and Luo, H. (2010). Thermochromic VO_2 thin films: Solution-based processing, improved optical properties, and lowered phase transformation temperature. Langmuir 26, 10738-10744.

209 Voti, R. L., Larciprete, M. C., Leahu, G., Sibilia, C., and Bertolotti, M. (2012).

Optical response of multilayer thermochromic VO_2-based structures. J. Nanophotonics 6, 61601.

210 Kang, L., Gao, Y., Chen, Z., Du, J., Zhang, Z., and Luo, H. (2010). Pt/VO_2 double-layered films combining thermochromic properties with low emissivity. Sol. Energy Mater. Sol. Cells 94, 2078-2084.

211 Du, J., Gao, Y., Chen, Z., Kang, L., Zhang, Z., and Luo, H. (2013). Enhancing thermochromic performance of VO_2 films *via* increased microroughness by phase separation. Sol. Energy Mater. Sol. Cells 110, 1-7.

212 Hendaoui, A., Emond, N., Chaker, M., and Haddad, E. (2013). Highly tunable-emittance radiator based on semiconductor-metal transition of VO_2 thin films. Appl. Phys. Lett. 102, 061107.

213 Saeli, M., Piccirillo, C., Parkin, I. P., Ridley, I., and Binions, R. (2010). Nano-composite thermochromic thin films and their application in energy-efficient glazing. Sol. Energy Mater. Sol. Cells 94, 141-151.

214 Saeli, M., Piccirillo, C., Parkin, I. P., Binions, R., and Ridley, I. (2010). Energy modelling studies of thermochromic glazing. Energy Build. 42, 1666-1673.

215 Chang, T., Cao, X., Dedon, L. R., Long, S., Huang, A., Shao, Z., Li, N., Luo, H., and Jin, P. (2018). Optical design and stability study for ultrahigh-performance and long-lived vanadium dioxide-based thermochromic coatings. Nano Energy 44, 256-264.

216 Kim, H., Kim, Y., Kim, K. S., Jeong, H. Y., Jang, A., Han, S. H., Yoon, D. H., Suh, K. S., Shin, H. S., Kim, T., and Yang, W. S. (2013). Flexible thermochromic window based on hybridized VO_2/graphene. ACS Nano 7, 5769-5776.

217 Yang, J., Xu, Z., Ye, H., Xu, X., Wu, X., and Wang, J. (2015). Performance analyses of building energy on phase transition processes of VO_2 windows with an improved model. Appl. Energy 159, 502-508.

218 Ye, H., Meng, X., and Xu, B. (2012). Theoretical discussions of perfect window, ideal near infrared solar spectrum regulating window and current thermochromic window. Energy Build. 49, 164-172.

219 Long, L. and Ye, H. (2014). How to be smart and energy efficient: A general discussion on thermochromic windows. Sci. Rep. 4, 6427.

220 Long, L. and Ye, H. (2014). Discussion of the performance improvement of thermochromic smart glazing applied in passive buildings. Sol. Energy 107,

236-244.

221 Ye, H. and Long, L. (2014). Smart or not? A theoretical discussion on the smart regulation capacity of vanadium dioxide glazing. Sol. Energy Mater. Sol. Cells 120, 669-674.

222 Ye, H., Long, L., Zhang, H., Xu, B., Gao, Y., Kang, L., and Chen, Z. (2013). The demonstration and simulation of the application performance of the vanadium dioxide single glazing. Sol. Energy Mater. Sol. Cells 117, 168-173.